Controlling competing photochemical reactions stabilises perovskite solar cells

Silvia G. Motti[1,2,5], Daniele Meggiolaro,[3,4] Alex J. Barker[1], Edoardo Mosconi,[4] Carlo Andrea Riccardo Perini[1,2], James M. Ball[1,5], Marina Gandini[1,2], Min Kim[1], Filippo De Angelis,[3,4,6*] Annamaria Petrozza[1*]

[1]Center for Nano Science and Technology @Polimi, Istituto Italiano di Tecnologia, via Giovanni Pascoli 70/3, 20133 Milan, Italy.

[2]Dipartimento di Fisica, Politecnico di Milano, Piazza L. da Vinci, 32, 20133 Milano, Italy.

[3]Computational Laboratory for Hybrid/Organic Photovoltaics (CLHYO), CNR-ISTM, Via Elce di Sotto 8, 06123, Perugia, Italy.

[4] D3-CompuNet, Istituto Italiano di Tecnologia, Via Morego 30, 16163 Genova, Italy.

[5]Current address: Department of Physics, University of Oxford, Clarendon Laboratory, Parks Road, Oxford, OX1 3PU, United Kingdom.

[6]Dipartimento di Chimica, Biologia e Biotecnologie, Università di Perugia, Via Elce di Sotto 8, I-06123 Perugia, Italy.

*Annamaria.petrozza@iit.it; filippo@thch.unipg.it

Abstract

Metal halide perovskites have been successfully applied as optically active layers in photovoltaics and in various optoelectronic devices. Long-term reliability must however be assured. Instabilities are manifested as light-induced ion migration and segregation, which can eventually lead to material degradation. Discordant reports have reported a beneficial role of ion migration under illumination, leading to defect healing. By combining *ab initio* simulations with photoluminescence measurements under controlled conditions, we demonstrate that photo-instabilities are related to light-induced formation and annihilation of defects acting as carrier trap states. We show that these phenomena coexist and compete. In particular, long-living carrier traps related to halide defects trigger photo-induced material transformations, which drive both processes. On short scales, defect annihilation can prevail over defect formation, which occurs on longer scales. Nevertheless, defect formation can be controlled by blocking under-coordinated surface sites, which act as a defect reservoir. By a specific surface passivation strategy we are thus able to stabilize the perovskite layer towards photo-induced instabilities, leading to improved optoelectronic material quality and enhanced photo-stability in a working solar cell.

The interest in metal halide perovskites has been growing continuously in recent years due to the remarkable evolution of their application in photovoltaics – that have reached power conversion efficiencies exceeding 23%[1] – as well as promising performance in light emitting diodes[2], photodetectors, and lasers[3,4]. This success owes much to their optimal optoelectronics properties, *i.e.* high absorption coefficients and long carrier lifetimes[5–7]. The soft nature of the lead-halide lattice induces relatively low defect formation energies, which implies a significant probability of defects formation[8]

through combined thermal- and light-induced phenomena. While the impact of defects seems not to be detrimental with respect to the figures of merit of perovskite-based devices,[9] their activity poses a challenge to the widespread uptake of perovskite-based optoelectronic devices in terms of material stability under electrical and optical stimuli.[10–14] Monitoring the photoluminescence (PL) and dynamics of photogenerated charge carriers is an effective approach for gathering information about the opto-electronic properties of a semiconductor. The PL efficiency is extremely sensitive to a combination of parameters such as recombination rate constants, defect densities, carrier lifetimes, and non-radiative decay paths; as such PL efficiency is usually taken as a measure of the material optoelectronic quality.

Since the primary function of lead halide perovskites in solar cells is to absorb light, the material response to light exposure and the possible associated phenomena are fundamental properties to enable reliable devices. A PL intensity decrease (PLID) has been observed in lead halide perovskite thin-films of different composition as a result of photo-induced trap formation in inert atmosphere[15]. Enhanced photo-induced ion migration[16] was interpreted as a defect density increase under light irradiation[17]. In direct contradiction, PL intensity enhancement (PLIE) under illumination has also been observed[18,19] which was explained by a light-induced trap annihilation mechanism.[20] A dependence of the PL efficiency variation on defect density[21] and excitation intensity[22] , with both PLIE and PLID, was reported. The atmosphere also has a strong impact on PL efficiency, with strong PLIE observed by exposing the sample to an oxygen-rich environment[15,23–27].

The presence of transient phenomena upon electrical and photo-excitation and a lack of understanding of the mechanisms behind such phenomena raise skepticism about the successful integration of lead halide perovskites in a reliable technology.

From a more fundamental point of view, no general consensus exists on whether the observed transient behaviors can eventually lead to an improved material quality or they can actually destroy the material.

Here we provide a comprehensive picture of the PLIE and PLID processes in methylammonium lead iodide ($MAPbI_3$) and bromide ($MAPbBr_3$) perovskites, showing that both phenomena can happen and compete in both materials by varying the illumination conditions, although with different characteristic times and temperature response.

Combining our observations with first-principles calculations we propose a model based on lead halide defect chemistry for both PLID and PLIE which consistently explains the overall phenomenology. We find that long-living carrier traps related to halide defects trigger photo-induced transformations which drive both PLIE and PLID. As long as the density of traps is relatively low or they are scarcely populated, photo-induced PLIE will be dominant. On the other hand, photo-induced PLID will take over in the presence of a high density of populated traps located close to thin film surface and grain boundaries, which provide a reservoir of binding sites for photo-generated species eventually leading to material degradation. Consistent with the developed model, we show that surface passivation of $MAPbI_3$ thin films allows us to switch off the PLID mechanism and make the PLIE process dominant, which translates into an associated solar cell efficiency increase and enhanced temporal stability.

Results

We monitored the PL intensity of $MAPbI_3$ and $MAPbBr_3$ perovskite thin-films used in efficient solar cell devices as a function of illumination time. Figure 1a shows the room temperature integrated PL over time of $MAPbI_3$ polycrystalline films deposited on

96 glass. The sample was excited with a laser beam incident on the film surface. The laser
97 was modulated with a fixed pulse width of 200 ns and varying repetition rate, *i.e.*
98 varying the period (δ) between two excitation pulses. The pulse energy was kept
99 constant to guarantee the same carrier generation density at each excitation pulse (in
100 Table S2 of SI the average excitation intensity as a function of δ are reported). To
101 exclude the effect of oxygen and moisture[15,24,25] all measurements were performed
102 under active vacuum (pressure $<10^{-5}$ mbar, under constantly running pump). We
103 observe that the PL intensity changes over time, showing both PLIE and PLID,
104 depending on the repetition rate for both $MAPbI_3$ and $MAPbBr_3$ (Figures 1a,c). At low
105 repetition rates -that is long δ, corresponding to the sample being in the dark for ~ms
106 time – the PL intensity cumulatively grows with subsequent illumination periods.
107 Increasing the repetition rate - short δ, corresponding to longer light exposure and less
108 time in the dark- a quenching process kicks in, which becomes eventually dominant
109 (Figures 1a,c). These observations clearly indicate that *light absorption can lead to*
110 *competing PLIE and PLID phenomena*, depending on the excitation conditions. We thus
111 performed additional experiments at varying temperatures to disentangle the factors
112 underlying the individual phenomena involved in PLIE and PLID. Figure 1b shows the
113 time evolution of the integrated PL intensity of a $MAPbI_3$ film excited with continuous-
114 wave (CW) light, analogous to a very high repetition rate, *i.e.* short δ, at different
115 temperatures. Each curve was taken on a fresh spot of the sample. For $MAPbI_3$, at 77 K
116 the PL is stable for the entire duration of the experiment, and the same holds when
117 heating the sample to 137 K. Further raising the temperature to 197 K we observe a
118 strong PLIE over time which is further boosted up to 237 K, leading to a factor of ~8 PL
119 increase compared to the initial value. At still higher temperature (277 K) an initial
120 PLIE is superseded by PLID at longer exposure times, which eventually dominates at

room temperature and above. Similar behavior was observed for $MAPbBr_3$ films upon varying the temperature, though with lower thresholds for PLID and PLIE (Figure 1c,d), making us safely exclude any role of structural phase transition in the observed dynamics (see also S27 in SI).

The PL intensity variations with increasing temperature and the transition from stable PL, to PLIE to PLID, is clearly suggestive of competing thermally activated processes that either improve or hinder the efficiency of radiative recombination. The dominant contribution of PLID at higher temperature suggests a higher energy demand for this process compared to PLIE. Also, the enhanced stability range of $MAPbI_3$ compared to $MAPbBr_3$ at low temperatures (cf. Figure 1b and 1d, with PLID starting at 277 and 197 K respectively) suggests that the threshold for switching between the two phenomena is determined by the precise material composition, in particular by the nature of the halide.

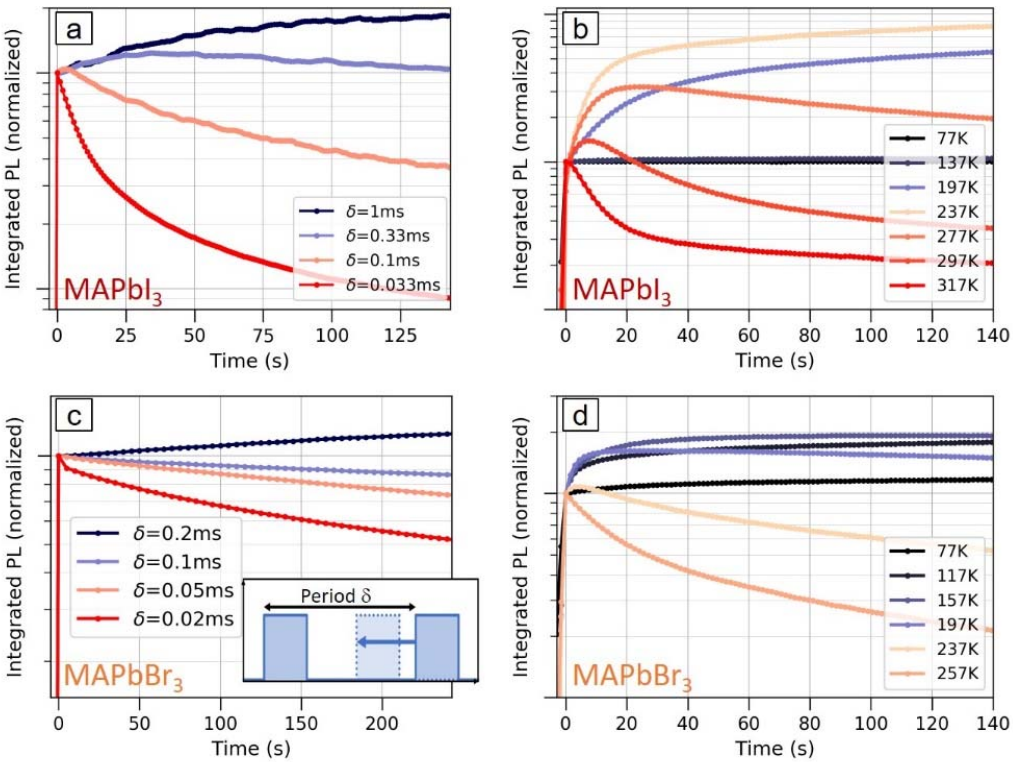

Figure 1 *a,c) Integrated PL intensity, normalized at time t=0, over time (excitation density ~1016 cm-3) on fresh spots of polycrystalline films of MAPbI3 (a) and MAPbBr3 (c) with increasing repetition rate (decreasing period δ) of the excitation light. The pulse width was fixed at 200 ns with constant pulse energy of 0.2 nJ (fluence ~0.5 μJ.cm^2, average intensity from 0.6 to 20 mW/cm^2, see also data with 10 μs pulse width shown in Fig S5). b-d) Integrated PL over time of MAPbI3 (b) and MAPbBr3 (d) at different temperatures under CW excitation (excitation intensity ~50mW/cm2). Excitation wavelength: 450 nm for MAPbI3 and 405nm for MAPbBr3.*

To identify what additional factors affect the PLID and PLIE processes, we investigated the PL time evolution of $MAPbI_3$ as a function of the excitation wavelength, as shown in Figure 2a. The incident photon density over the illuminated spot area was kept constant, and each curve was taken on a fresh spot of the film. We observe that PLID is significantly enhanced at shorter excitation wavelengths, while band-edge excitation results in more stable PL. Besides the additional thermal energy provided by above-gap

excitation, shorter wavelength light also has significantly shorter penetration depth (Figure 2b). This results in a higher carrier generation close to the film surface, with a factor ~2 increase in the first 30 nm film away from the surface in case of 480 *vs.* 750 nm excitation. While we cannot exclude direct excitation of PbI_2 as the cause of PLID and PLIE,[27] the observation of both phenomena for $MAPbBr_3$ is consistent with a minor role of this phenomenon in our conditions, as excitation of the higher band-gap (~4 eV) $PbBr_2$ phase only occurs at much shorter excitation wavelength than those used in our experiments. Our observations suggest that the competition between PLID and PLIE is strongly related to the illumination conditions of the thin film which may include factors such as proximity to the reactive surface, uniformity of the excitation profile, and excitation density, with possible contribution of thermal dissipation effects following photo-excitation.

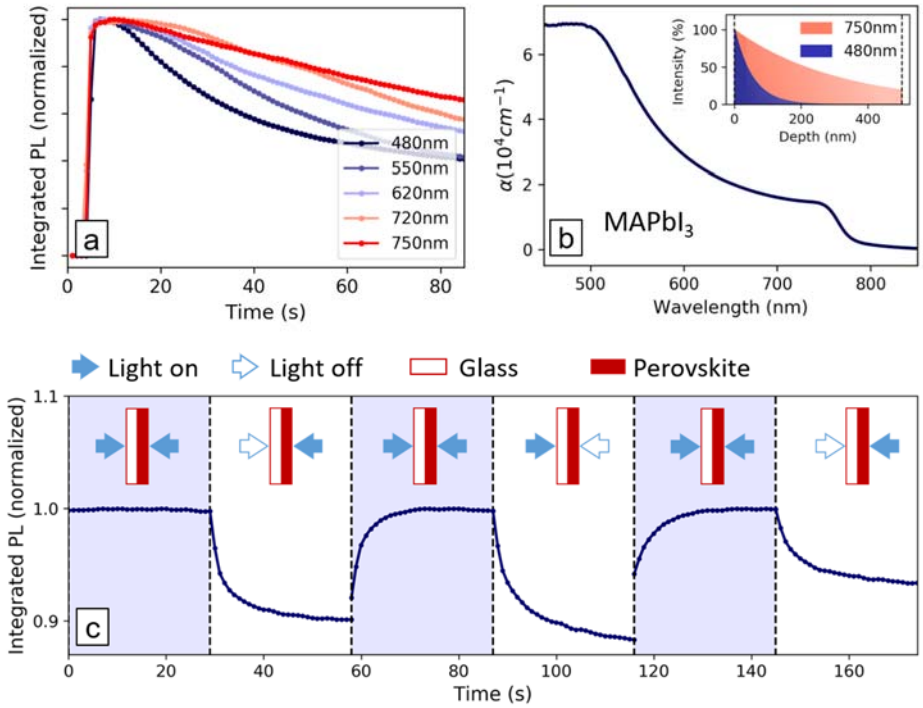

Figure 2. *(a) Integrated PL over time obtained using excitation light of different wavelengths. (b) Absorption spectrum of $MAPbI_3$ thin film (see absorbance in S28) and photoexcitation profiles when using 480 nm or 750 nm light (inset). (c) Integrated PL*

165 *intensity over time of a $MAPbI_3$ film on glass. Excitation is performed at 560 nm with*
166 *symmetrical beams of equal intensity impinging on both the perovskite and glass side of*
167 *the sample. Each section of the time trace is normalized by its maximum intensity for*
168 *visualization purpose (See Figure S6 in SI for unnormalized data).*
169
170 To complement our phenomenological consideration, we investigated whether the
171 experiment geometry could affect the relative weight of PLID *vs.* PLIE. We find a
172 reproducible PLIE when illuminating the film from two sides (the open surface and the
173 glass side) with two identical beams covering a large area of the thin film, suggesting
174 that a uniform illumination may reduce the impact of PLID (Figure 2c). Similar
175 observations, *i.e.* a switch from PLID to a more stable PL is also observed by varying
176 the lateral illumination gradient (see Supplementary Information Figure S7).
177 To provide a rationale for these observations we first consider the possible role
178 of trap-state filling, followed by de-trapping, as a possible cause determining the
179 observed phenomenology. Despite the long lifetimes of trapped carriers in both $MAPbI_3$
180 and $MAPbBr_3$ [9,15,28], extending up to several μs, the timescales spanned by the repetition
181 rates in Figures 1a,c are too long to be solely explained by trapping/de-trapping
182 mechanisms. The system can reach almost a stationary density of charge carriers within
183 the 200 ns pulse (see Supplementary Information, Figure S2-S4 and S22-S25, for
184 simulations of charge carrier dynamics under CW or modulated illumination. Please
185 note that the change in modulation mainly results in a change in the averaged excitation
186 intensity and an enhancement of the PL absolute value at time t=0, due to an associated
187 enhancement of counts during the integration, see Fig S26 in SI); if no concomitant
188 processes take place, though, the ms delay time between two consecutive pulses allows
189 the system to return to the ground state before a second pulse comes, in contrast to the

190 cumulative effect of pulsed illumination observed in Figure 1a,c. Likewise,
191 charge/lattice interaction through formation of large polarons[29] show lifetimes
192 comparable to those of the charge carriers, inconsistent with the cumulative effect
193 observed with ms delay. Similarly, we can rule out a role of light induced release of
194 lattice strain[30] in PLE, since electronic effects are too fast to provide a cumulative effect
195 on the ms repetition time scale of our experiments.

196 The time scales involved in PLID and PLIE are consistent with the reported
197 ionic activities, such as ion/defect annihilation and migration rates, in both $MAPbI_3$ and
198 $MAPbBr_3$,[20,31] and with the time scale of photo-induced transformations in free standing
199 $MAPbI_3$ films.[32] Comparably, in mixed halide (I, Br) perovskites ion segregation was
200 shown to take place via halide defects, mainly vacancies and interstitials, driven by the
201 gradient in carrier generation through the thickness of these strongly absorbing
202 materials[33–35]. Importantly, Tthe observation of typical spectral features associated with
203 trap carriers and defects in the lattice that are enhanced under illumination (see
204 Supplementary Information Figure S8 and S9) is suggestive of photo-induced defect
205 formation and annihilation being respectively related to PLID and PLIE.

206 With the aid of first-principles calculations we propose a model based on lead-
207 halides defect chemistry which allows us to consistently explain the observations of the
208 data set presented above. $MAPbI_3$ and $MAPbBr_3$ show a remarkably similar defect
209 chemistry (see Supplementary Information for comparative analysis based on hybrid
210 DFT calculations including spin-orbit coupling) which is dominated by lead vacancies
211 (V_{Pb}) and interstitial halogen (I_i or Br_i) defects. We henceforth use the notation for
212 defects in $MAPbI_3$ (*e.g.* I_i), but the mechanism applies similarly to $MAPbBr_3$. We
213 notice, however, that for the latter the involved defects are somehow shallower than in
214 $MAPbI_3$ (see Supplementary Information Figure S10). Both halide interstitials and lead

vacancies show thermodynamic ionization levels in the band gap. At the calculated native Fermi level V_{Pb} is stable in the 2- charge state, thus this defect could trap holes by the (-/2-) transition level whose energy falls 0.13 eV above the VB, while I_i^- exhibits a (0/-) charge transition 0.29 eV above the VB. The partial shallow character of V_{Pb} transition, less deep than I_i, and the high migration barriers associated to the diffusion of the defect (Ea~1.0 eV)[36] highlight that this defect is only moderately active as a trap, while I_i can significantly trap both electrons and holes (see Supplementary Information Figure S10) through the (+/0) and (0/-) transitions. Hole trapping/de-trapping at I_i^- is a relatively fast process, while electron trapping at I_i^+ induces long living states due to the strong associated geometrical relaxation decreasing the kinetics of electron detrapping[9,28]. The promoter of possible material transformations must be a long-living species, whose formation may trigger subsequent photo-chemical transformations leading to both PLID and PLIE. The most natural candidates are thus the filled electron traps with their associated μs lifetime.

Recombination of I_i^- with V_I^+ was proposed as a mean of trap annihilation [20], which restores the pristine material and decreases the concentration of traps, thus it can be associated to PLIE. Here we further disclose that long living electrons at trapped I_i^+ defects may additionally mediate Frenkel defect annihilation.

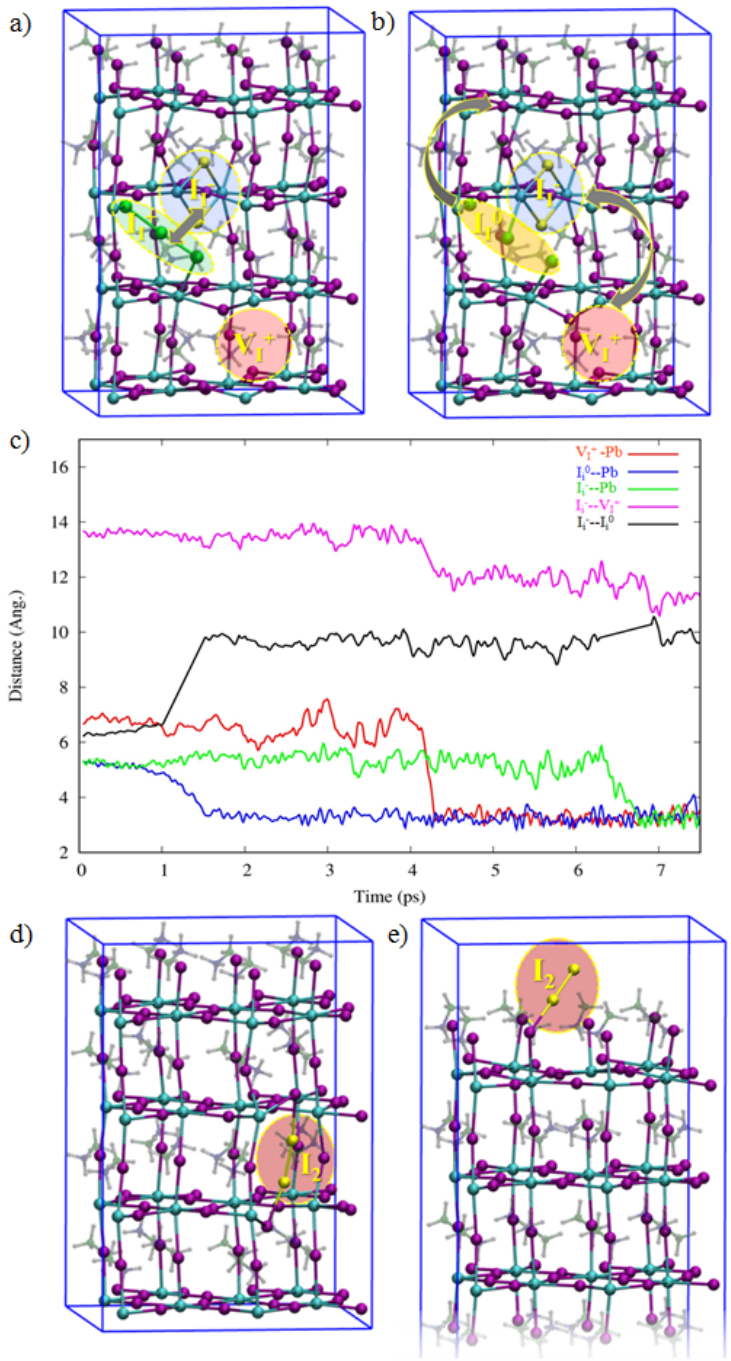

Figure 3. *a) Optimized structure of the interacting (as signaled by the arrow) I_i^+/I_i^- defect pair (shaded green and blue areas, respectively) and a distant V_I^+ defect (shaded red area). The formation of the I_i^---V_I^+ defects in the presence of an interacting I_i^+ is endothermic by 0.55 eV. b) Electron trapped at I_i^+ to form I_i^0/I_i^- defect pair (shaded orange and blue areas, respectively). The arrows indicate the direction of I_i^0 migration and I_i^---V_I^+ annihilation. The formation of the I_i^---V_I^+ defects in the presence of a*

neutral I_i^0 is endothermic by 0.86 eV. c) Dynamical evolution of the system after electron trapping at I_i^+. A sequence of ion reorganization and migration events can be visualized: 1) following electron trapping at I_i^+, the system rapidly reaches the minimum energy structure of I_i^0 (blue line) increasing the I_i^0/ I_i^- distance (black line); 2) V_I^+ migrates in the direction of I_i^- (red and magenta lines); 3) I_i^- further migrates in the direction of V_I^+ (green and magenta lines). d) Optimized structure of an unstable bulk I_2 molecule (dark red shaded area), which migrates to the perovskite (001) surface in e) to form a stable surface bound I_2 molecule (dark red shaded area). Binding of an I_2 molecule to the perovskite surface (bulk) is exothermic (endothermic) by 0.48 (0.40) eV.

Briefly, the formation of a I_i^---V_I^+ Frenkel pair in the presence of a neighboring I_i^+ is endothermic by 0.55 eV since this process requires to break a Pb-I bond and displacing the I_i^---V_I^+ defects away, Figure 3a. Upon electron trapping at I_i^+, which is preferentially located next to I_i^-, the system is further destabilized by 0.31 eV, Figure 3b, adding a significant driving force to restore the pristine material. The long-living nature of the formed I_i^0, which mirrors the long electron de-trapping time, may allow sufficient time for I_i^---V_I^+ annihilation to effectively take place. Further insight on such process was obtained by *ab initio* molecular dynamics. We start from the minimum energy geometry of I_i^---V_I^+ Frenkel pair interacting with I_i^+ (Figure 3a) and add one electron to the system, following the dynamical evolution of this globally neutral system. A sequence of ion reorganization and migration events can be visualized: 1) following electron trapping at I_i^+, confirmed by spin localization at the defect site, the system rapidly reaches the minimum energy structure of I_i^0 (blue line in Figure 3c) increasing the I_i^0/ I_i^- distance (black line); 2) V_I^+ migrates in the direction of I_i^- (red and magenta lines); 3) I_i^- further migrates in the direction of V_I^+ (green and magenta lines). The results are

266 consistent with electron trapping at I_i^+ promoting I_i^---V_I^+ annihilation, as inferred from
267 the two oppositely charged defects migrating towards each other twice within less than
268 10 ps. A simulation starting from the same structure but with no added electron at I_i^+ did
269 not show any shortening of the I_i^---V_I^+ distance, though the I_i^+ / I_i^- defects jointly
270 migrated in the investigated time, see Supporting Information Figure S11.
271 The light-induced PLIE process can be schematized as follows:
272 I_i^+/ I_i^---V_I^+ + 1e → I_i^0 / I_i^---V_I^+ → I_i^0 + *prist* eq. 1
273 where *prist* represents the pristine material. Annihilation of the I_i^---V_I^+ Frenkel pair is
274 entropically disfavored, with a small energy barrier related to the migration of I_i^- and
275 V_I^+ (~0.1 eV)[37]. This reaction is thus favored at low temperature but it still requires a
276 sufficient thermal energy to accomplish defect migration.
277 The detrapping reaction:
278 I_i^0 → I_i^++ 1e eq. 2
279 instead has a significant activation energy (0.29 eV)[9], so the annihilation process of
280 eq.1, mediated by the high ion mobility of iodine defects, can effectively prevail over
281 the thermally activated detrapping of eq.2. Such PLIE mechanism is fully consistent
282 with the data of Figure 1b,d, showing a preferential PLIE at low temperature but no
283 PLIE if the temperature is too low to hamper defect migration. In the absence of other
284 (PLID) processes this PLIE mechanism is cumulative since it requires a long time after
285 de-trapping to restore the initial density of Frenkel defects due to the endothermic
286 nature of the process, with the possible associated entropic gain hindered at low
287 temperature. By definition, in a Frenkel defect an ion leaves its place in the lattice,
288 creating a vacancy, and it becomes an interstitial by lodging in a nearby location, thus
289 we expect to observe their annihilation happening even when only short-range
290 migration is allowed (*e.g.* at low temperature).

The PLID process is likely more complex than PLIE. We know that PLID is favored by high illumination repetition rates. This is in turn associated with a larger fraction of traps being filled at any time, and possibly to a higher effective temperature due to heating of the sample. We also know from the wavelength dependence of PLID that this process is more efficient when the photo-generation happens close to the surface where a larger trap density can be envisaged. It is also amplified when ion diffusion is enhanced, *i.e.* by the presence of gradient across dark/light regions.

A possible PLID mechanism could thus be reasonably associated to a bimolecular reaction – boosted by increasing the encountering probability of the reactants, *i.e.* by increasing their density and/or their mobility – occurring among the filled, long living traps, in a film region close to the surface. Following the initiating trap filling reaction of eq. 2, two filled traps could react to form an I_2 molecule:

$$2\ I_i^0 \rightarrow I_2 \qquad \text{eq. 3.}$$

This radical quenching reaction, involving two coordinated I_2^- molecules,[38] takes place virtually with no energy barrier (Supplementary Information Figure S12) being it only limited by diffusion of the reactants. Such bimolecular reaction is favored by a high trap concentration in a small volume that increases the probability of a bimolecular encounter, as realized by high irradiation intensity of short wavelength, as well as by allowing for long-range I_i^0 migration. The direct recombination of two interacting I_i^-/I_i^+ defects to give I_2 has instead a fairly high activation energy (0.33 eV, when calculated among surface-adsorbed species, see Supporting Information Figure S13).

Sequential electron and hole trapping could alternatively take place at the I_i^+/ I_i^- defect pair:

$$I_i^+/ I_i^- + 1e \rightarrow I_i^0 / I_i^- + 1h \rightarrow 2I_i^0 \rightarrow I_2 \qquad \text{eq. 4}$$

The last reaction step leads to the same I_2 product as eq. 3 but its reaction probability is likely limited by the short living trapped hole at I_i^-.

A filled trap may also take a second electron to form I_i^-:

$I_i^0 + 1e \rightarrow I_i^-$ eq. 5.

the bielectronic reaction in eq. 5 is favored by high irradiation intensity. Formation of I_2 is possibly favored over capture of a second electron, but both mechanisms can coexist. I_2 loss into toluene solution following $MAPbI_3$ light irradiation was recently reported [17], consistent with eq.3 and 4. I_2 can be trapped as a complex in the bulk (formally I_4^{2-}, Figure 3d) or it may disproportionate to reform the I_i^+/ I_i^- pair [37,39]. Importantly, both coordinated I_2 and the I_i^+/ I_i^- pair tend to migrate to the surface, being stabilized by ~0.4 eV. A surface-coordinated I_2 molecule represents the final reaction product (Figure 3e). Such I_2 molecule can remain bound to the surface or to grain boundaries. Notably I_2 can act as an electron trap, as I_i^+ does.

The iodine imbalance between surface and bulk can trigger a series of compensating reactions that regenerate the starting equilibrium distribution of I_i^+/ I_i^- defects to compensate their transformation to surface bound I_2. This can be accomplished by disrupting the pristine lattice as

$prist \rightarrow V_{Pb2}^- + V_I^+ + I_i^+$ eq. 6

or through formation of Frenkel pairs, according to eq.1, here simplified as

$prist \rightarrow V_I^+ + I_i^-$ eq. 1'

or the net reaction:

$prist \rightarrow V_{Pb}^{2-} + 2V_I^+ + I_i^- + I_i^+$ eq. 7.

Note that $V_{Pb}^{2-} + 2V_I^+$ corresponds to the loss of PbI_2, which may segregate as a separate phase, with consequent material degradation[40] and associated PLID. Alternatively, metallic Pb could nucleate on the material surfaces[41].

The trigger to PLID is thus the surface (or grain boundary) stabilization of coordinated I_2. Treating the thin film with appropriate passivating agents and *blocking undercoordinated surface Pb atoms is thus the key to avoid PLID*[42]. Surface passivation will result not only in an improvement of the absolute PL quantum yield of the semiconductor thin film (surface-bound I_i^- is destabilized when the $MAPbI_3$ surface is capped by aliphatic ethers, see Supplementary Information Figure S14) but also in hampering the PLID phenomenon, leaving room for PLIE to happen.

The key to block PLID and likely to significantly slow down perovskite degradation is the passivation of surface sites to which I_2 can bind in its various forms. These undercoordinated Pb surface sites, not directly involved in trapping/detrapping events, act as a reservoir for I_2, leading to iodine imbalance in the bulk and stimulating the production of additional defects. The process continues until surface sites are saturated, after which the material may start releasing I_2 and possibly form a segregated PbI_2 phase. Scheme 1 summarizes the PLIE and PLID mechanisms.

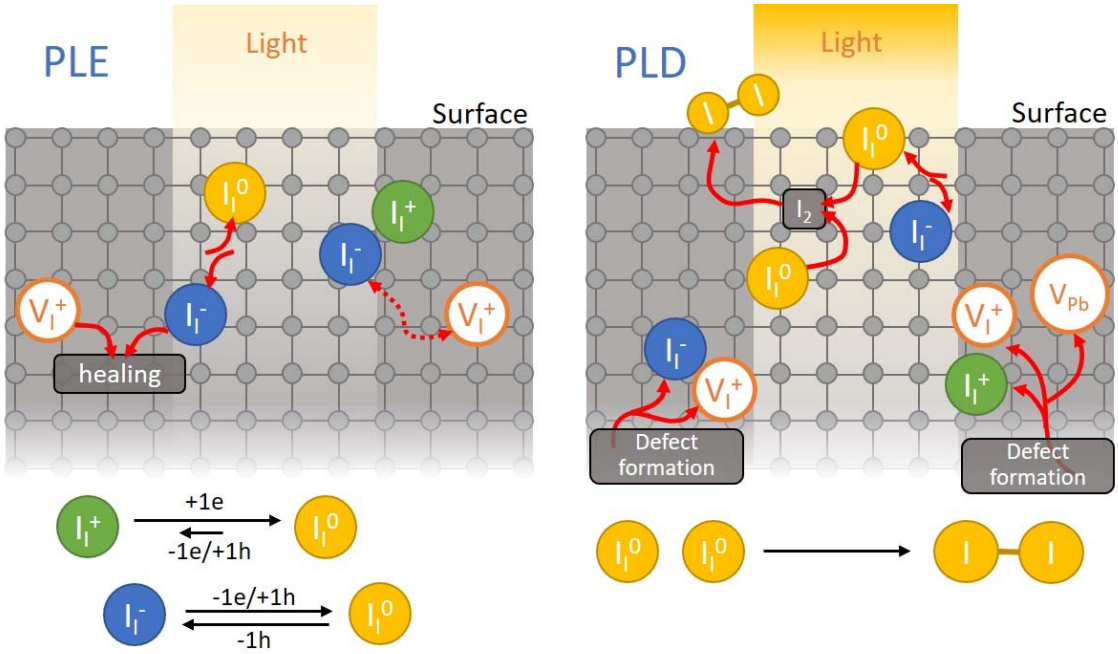

Scheme 1. Ion migration promoting PLID and PLIE in $MAPbI_3$ thin film.

357 To check the importance of the surface in PLID, we compared a pristine
358 $MAPbI_3$ film with one coated with tri-n-octylphosphine oxide (TOPO) or polyethylene
359 oxide (PEO) (Figure 4a). TOPO has been applied for the passivation of perovskite films
360 resulting in enhanced PL efficiencies and lifetimes.[7] PEO is a polymer containing polar
361 ether groups and hydroxyl terminations, representing a moisture barrier and a possible
362 passivating agent[43,44]. In Figure 4a, by illuminating a fresh spot of the samples (560 nm,
363 CW excitation, fluence of ~0.1 μJcm^{-2}) and monitoring the integrated PL signal over a
364 few minutes we observed a slow quenching for the bare $MAPbI_3$ thin film and an initial
365 enhancement followed by a slower quenching for the TOPO passivated thin film. On
366 the other hand, in the presence of PEO we observe that the mechanism leading to PLID
367 is switched off even at room temperature (Figure 4b). Despite TOPO and PEO are both
368 characterized by the presence of oxygen atoms which interact with undercoordinated
369 surface Pb atoms, (see Supplementary Information Figure S14) the increased PLIE
370 observed with PEO is suggestive of a more effective passivation by the latter, probably
371 because of the larger fraction of oxygen atoms against aliphatic carbon chains in PEO.
372 Figure 4b shows the relative PL quantum yield, calculated as the integrated PL intensity
373 normalized by the excitation intensity, of $MAPbI_3$ films. Each data point was taken after
374 a hold time of ~30 seconds. When measuring from low to high excitation intensities
375 (solid lines) and then in reverse order (dashed lines), we observe a hysteretic behavior
376 resulting from photoinduced trap formation, *i.e.* PLID and a concomitant PL intensity
377 reduction from bare perovskite thin films. By illuminating the film from the passivated
378 side, both the TOPO and PEO coated samples show a higher PL signal, indicating a
379 decrease in the density of native defects on the thin film surface. Thus, also in
380 agreement with the data shown in Figure 4a, the sample coated with TOPO shows a less
381 pronounced hysteretic behavior compared to the uncoated film, while the PEO

passivated thin film presents an opposite hysteretic behavior of the relative PL as a function of excitation intensity, as a consequence of a dominant PLIE process. This clearly shows that efficient surface passivation can reduce the density of defect states and photo-stabilize the perovskite thin film. To connect our experimental and computational model, in particular the central role of surface-stabilized I_2 in PLID, we investigated the I_2-releasing reaction in hexane solution from $MAPbI_3$ films considering three cases: i) the bare thin film; ii) $MAPbI^3$ capped by an inert polystyrene film; and iii) a PEO-passivated film. In line with the results of Kim et al.[17] prolonged irradiation of the bare $MAPbI_3$ and polystyrene-capped thin films produced the same amount of I_2, while a significant reduction in I_2 production was observed for the PEO-passivated thin film (Supplementary Figures S18-S20).

The passivating PEO layer has a significant technological relevance as it allows for the formation of high quality interlayer thin films which can be easily implemented in perovskite solar cells. In Figure 4c we show the J-V characteristic of $MAPbI_3$ based solar cells. Here we add PEO interlayers between the perovskite active layer and the selective charge extracting layers. The PEO layer is seen to improve the open circuit voltage (V_{OC}) when applied to either the electron- or hole-extracting interface, with the best performance given by the device with PEO applied to both sides (see the devices figure of merit in Table S1 and their statistics in Figure S15 of the SI). In Figure 4.d we show the evolution of the V_{OC} of solar cells with and without the PEO interlayers under one sun illumination (see Figure S17 of SI for monochromatic photo-excitation). The devices were encapsulated in inert atmosphere. Despite the fact that the perovskite layer in the reference device is already interfaced with materials which have, to some extent a passivating role, such as C_{60}[45,46], we still see competing dynamics in the Voc which mirror the PLID and PLIE shown in Figure 4.a. However, the relative contribution of

407 the PLID is drastically reduced in the PEO-treated device, resulting in a higher and

408 more stable Voc.

409

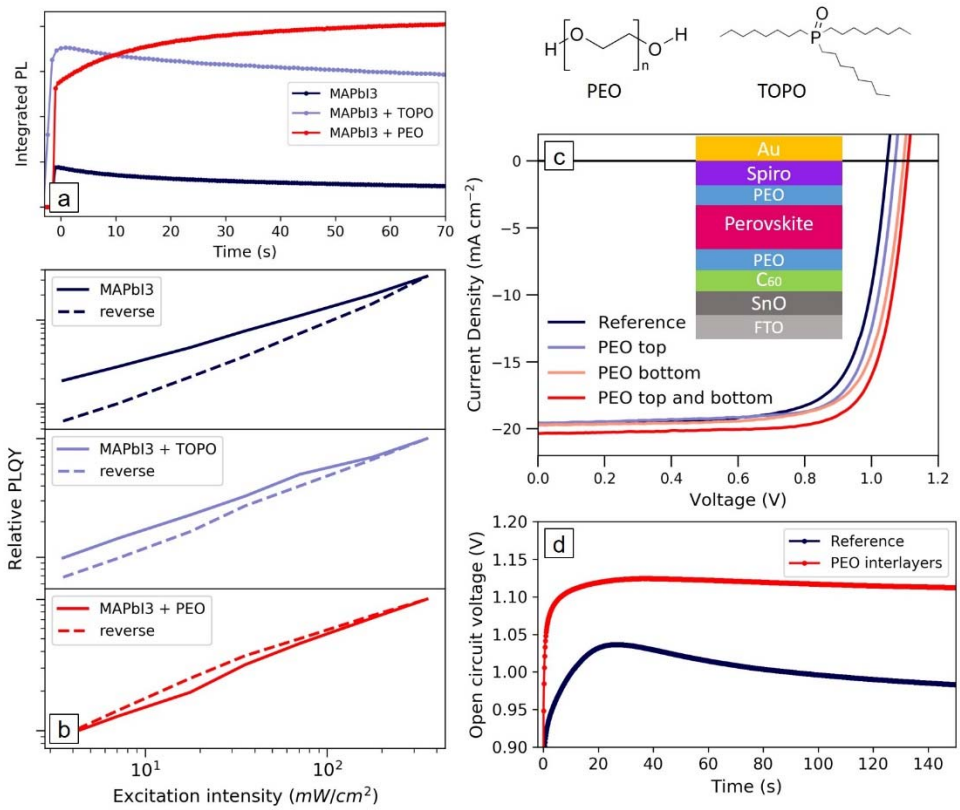

410

411

412 **Figure 4**. *(a) PL intensity over time of the $MAPbI_3$ films bare (blue) and coated with*

413 *TOPO (light blue) or PEO (red), taken on fresh spots (560 nm, CW, 40mW cm^{-2}); (b)*

414 *Relative PLQY, taken with increasing (solid lines) or decreasing (dashed lines)*

415 *excitation intensities (CW illumination, 560 nm, hold time between data points*

416 *~30 seconds) of $MAPbI_3$ thin films bare (dark blue) and coated with TOPO (light blue)*

417 *or PEO (red); (c) Current density voltage (J–V) curves measured under 1 sun of*

418 *$MAPbI_3$ devices with and without PEO interlayers; (d) open-circuit voltage (Voc)*

419 *transient measured from solar cells with and without PEO interlayers under one sun*

420 *illumination.*

421

Most notably, the PEO-passivated device shows also significantly longer stability under light soaking at the maximum power point, retaining more than 90% of its initial efficiency for15h; while the bare $MAPbI_3$ device looses 35% of its initial efficiency within the first 6h, see Supplementary Figure S21.

It is worth to mention that LEDs may operate at a relatively high density of carriers, thus they may suffer more from the PLID mechanism. As we have demonstrated, PEO interlayers are capable of passivating the perovskite surfaces minimizing the formation of degradation products (*i.e.* I_2) without blocking the charge injection in the device. Therefore we believe PEO could be beneficial to LED stability too.

In conclusion, by monitoring the evolution of PL intensity under systematic control of the experimental parameters we identified two distinct processes behind the instabilities observed in lead halide perovskites, excluding effects related to the atmosphere. We demonstrate that such processes are simultaneously happening within the thin films under photo-excitation, and that depending on the conditions, one can overcome the other, conciliating the conflicting reports in literature and providing a consistent understanding of photoinduced phenomena in this class of materials. Based on simple yet comprehensive experimental evidence we are able to provide a clear model, in which long-living trapped carriers – typical of halide photochemistry - mediate photo-induced ionic dynamics which can lead to a dominant PL enhancement or decrease. The latter stems from a bimolecular reaction which due to the encounter of two I^0 species to form I_2, thus it is favored in the presence of high trap density concentration and/or high temperature. The stabilization of coordinated I_2 at the surface (or grain boundary) is a fundamental factor for the efficiency loss. On such grounds, we show that passivating the thin film surface prevents the detrimental process leading to PL decrease, favoring the defect healing. This allows us to target the relevant defect

sites by passivating the semiconductor surface with PEO interlayers, improving device performance and stability.

ACKNOLEDGEMENTS

This work has been funded by the European Union project PERT PV under grant agreement n° 763977, and ERC project SOPHY under grant agreement N 771528 S.G.M. thanks the CNPq (Conselho Nacional de Desenvolvimento Científico e Tecnológico - Brasil) for the scholarship [206502/2014-1]. The authors thank Dr Giuseppe Paternò for his support to set-up the transient Voc characterization.

AUTHOR CONTRIBUTIIONS

S.G.M. performed the PL measurements, D.M. and E.M. performed the first-principle calculations, A.R.P., J.M.B, M.G. and M.K. were responsible for the thin films fabrication, M.K. fabricated the solar cell devices and M.K and A.J.B characterized the solar cell. A.P., S.M, A.J.B., D.M. and F.D.A. analyzed the data. S.G.M, F.D.A. and A.P. wrote the first draft of the manuscript and all authors contributed with the discussions and finalized the manuscript. AP supervised the project.

COMPETING INTERESTS

The authors declare no competing interests.

REFERENCES

(1) NREL. Best Research-Cell Efficiencies

https://www.nrel.gov/pv/assets/images/efficiency-chart.png (accessed May 23, 2018).

(2) Li, G.; Tan, Z.-K.; Di, D.; Lai, M. L.; Jiang, L.; Lim, J. H.-W.; Friend, R. H.; Greenham, N. C. Efficient Light-Emitting Diodes Based on Nanocrystalline Perovskite in a Dielectric Polymer Matrix. *Nano Lett.* **2015**, *15* (4), 2640–2644.

(3) Zhu, H.; Fu, Y.; Meng, F.; Wu, X.; Gong, Z.; Ding, Q.; Gustafsson, M. V; Trinh, M. T.; Jin, S.; Zhu, X.-Y. Lead Halide Perovskite Nanowire Lasers with Low Lasing Thresholds and High Quality Factors. *Nat. Mater.* **2015**, *14* (6), 636–642.

(4) Deschler, F.; Price, M.; Pathak, S.; Klintberg, L. E.; Jarausch, D.-D.; Higler, R.; Hüttner, S.; Leijtens, T.; Stranks, S. D.; Snaith, H. J.; Atatüre, M.; Phillips, R. T.; Friend, R. H. High Photoluminescence Efficiency and Optically Pumped Lasing in Solution-Processed Mixed Halide Perovskite Semiconductors. *J. Phys. Chem. Lett.* **2014**, *5* (8), 1421–1426.

(5) Stranks, S. D.; Eperon, G. E.; Grancini, G.; Menelaou, C.; Alcocer, M. J. P.; Leijtens, T.; Herz, L. M.; Petrozza, A.; Snaith, H. J. Electron-Hole Diffusion Lengths Exceeding 1 Micrometer in an Organometal Trihalide Perovskite Absorber. *Science (80-.).* **2013**, *342* (6156), 341–344.

(6) Johnston, M. B.; Herz, L. M. Hybrid Perovskites for Photovoltaics: Charge-Carrier Recombination, Diffusion, and Radiative Efficiencies. *Acc. Chem. Res.* **2016**, *49* (1), 146–154.

(7) deQuilettes, D. W.; Koch, S.; Burke, S.; Paranji, R.; Shropshire, A. J.; Ziffer, M. E.; Ginger, D. S. Photoluminescence Lifetimes Exceeding 8 Ms and Quantum Yields Exceeding 30% in Hybrid Perovskite Thin Films by Ligand Passivation. *ACS Energy Lett.* **2016**, *1* (2), 1–7.

(8) Ball, J. M.; Petrozza, A. Defects in Perovskite-Halides and Their Effects in Solar

Cells. *Nat. Energy* **2016**, *1* (11), 16149.

(9) Meggiolaro, D.; Motti, S.; Mosconi, E.; barker, A.; Ball, J.; Perini, C. A. R.; Deschler, F.; Petrozza, A.; De Angelis, F. Iodine Chemistry Determines the Defect Tolerance of Lead-Halide Perovskites. *Energy Environ. Sci.* **2018**, *11* (3), 702–713.

(10) Hoke, E. T.; Slotcavage, D. J.; Dohner, E. R.; Bowring, A. R.; Karunadasa, H. I.; McGehee, M. D. Reversible Photo-Induced Trap Formation in Mixed-Halide Hybrid Perovskites for Photovoltaics. *Chem. Sci.* **2014**, *6* (1), 613–617.

(11) Sanchez, R. S.; Gonzalez-Pedro, V.; Lee, J.-W.; Park, N.-G.; Kang, Y. S.; Mora-Sero, I.; Bisquert, J. Slow Dynamic Processes in Lead Halide Perovskite Solar Cells. Characteristic Times and Hysteresis. *J. Phys. Chem. Lett.* **2014**, *5* (13), 2357–2363.

(12) Leijtens, T.; Hoke, E. T.; Grancini, G.; Slotcavage, D. J.; Eperon, G. E.; Ball, J. M.; De Bastiani, M.; Bowring, A. R.; Martino, N.; Wojciechowski, K.; McGehee, M. D.; Snaith, H. J.; Petrozza, A. Mapping Electric Field-Induced Switchable Poling and Structural Degradation in Hybrid Lead Halide Perovskite Thin Films. *Adv. Energy Mater.* **2015**, *5* (20), 1–11.

(13) Gottesman, R.; Gouda, L.; Kalanoor, B. S.; Haltzi, E.; Tirosh, S.; Rosh-Hodesh, E.; Tischler, Y.; Zaban, A.; Quarti, C.; Mosconi, E.; De Angelis, F. Photoinduced Reversible Structural Transformations in Free-Standing CH<inf>3</Inf>NH<inf>3</Inf>PbI<inf>3</Inf> Perovskite Films. *J. Phys. Chem. Lett.* **2015**, *6* (12), 2332–2338.

(14) Gottesman, R.; Zaban, A. Perovskites for Photovoltaics in the Spotlight: Photoinduced Physical Changes and Their Implications. *Acc. Chem. Res.* **2016**, *49* (2), 320–329.

522 (15) Motti, S. G.; Gandini, M.; Barker, A. J.; Ball, J. M.; Srimath Kandada, A. R.;
523 Petrozza, A. Photoinduced Emissive Trap States in Lead Halide Perovskite
524 Semiconductors. *ACS Energy Lett.* **2016**, *1* (4), 726–730.
525 (16) Xing, J.; Wang, Q.; Dong, Q.; Yuan, Y.; Fang, Y.; Huang, J. Ultrafast Ion
526 Migration in Hybrid Perovskite Polycrystalline Thin Films under Light and
527 Suppression in Single Crystals. *Phys. Chem. Chem. Phys.* **2016**, *18* (44), 30484–
528 30490.
529 (17) Kim, G. Y.; Senocrate, A.; Yang, T. Y.; Gregori, G.; Grätzel, M.; Maier, J. Large
530 Tunable Photoeffect on Ion Conduction in Halide Perovskites and Implications for
531 Photodecomposition. *Nat. Mater.* **2018**, *17* (5), 445–449.
532 (18) deQuilettes, D. W.; Zhang, W.; Burlakov, V. M.; Graham, D. J.; Leijtens, T.;
533 Osherov, A.; Bulović, V.; Snaith, H. J.; Ginger, D. S.; Stranks, S. D. Photo-Induced
534 Halide Redistribution in Organic–inorganic Perovskite Films. *Nat. Commun.* **2016**,
535 *7*, 11683.
536 (19) Stranks, S. D.; Burlakov, V. M.; Leijtens, T.; Ball, J. M.; Goriely, A.; Snaith, H. J.
537 Recombination Kinetics in Organic-Inorganic Perovskites: Excitons, Free Charge,
538 and Subgap States. *Phys. Rev. Appl.* **2014**, *2* (3), 034007.
539 (20) Mosconi, E.; Meggiolaro, D.; Snaith, H. J.; Stranks, S. D.; De Angelis, F. Light-
540 Induced Annihilation of Frenkel Defects in Organo-Lead Halide Perovskites.
541 *Energy Environ. Sci.* **2016**, *9* (10), 3180–3187.
542 (21) Chen, S.; Wen, X.; Huang, S.; Huang, F.; Cheng, Y.-B.; Green, M.; Ho-Baillie, A.
543 Light Illumination Induced Photoluminescence Enhancement and Quenching in
544 Lead Halide Perovskite. *Sol. RRL* **2017**, *1* (1), 1600001.
545 (22) Hong, D.; Zhou, Y.; Wan, S.; Hu, X.; Xie, D.; Tian, Y. Nature of Photo-Induced
546 Quenching Traps in Methylammonium Lead Triiodide Perovskite Revealed by

Reversible Photoluminescence Decline. *ACS Photonics* **2018**, acsphotonics.7b01537.

(23) Fang, H.-H.; Adjokatse, S.; Wei, H.; Yang, J.; Blake, G. R.; Huang, J.; Even, J.; Loi, M. A. Ultrahigh Sensitivity of Methylammonium Lead Tribromide Perovskite Single Crystals to Environmental Gases. *Sci. Adv.* **2016**, *2* (7), e1600534–e1600534.

(24) Galisteo-López, J. F.; Anaya, M.; Calvo, M. E.; Míguez, H. Environmental Effects on the Photophysics of Organic-Inorganic Halide Perovskites. *J. Phys. Chem. Lett.* **2015**, *6* (12), 2200–2205.

(25) Tian, Y.; Peter, M.; Unger, E.; Abdellah, M.; Zheng, K.; Pullerits, T.; Yartsev, A.; Sundström, V.; Scheblykin, I. G. Mechanistic Insights into Perovskite Photoluminescence Enhancement: Light Curing with Oxygen Can Boost Yield Thousandfold. *Phys. Chem. Chem. Phys.* **2015**, *17* (38), 24978–24987.

(26) Meggiolaro, D.; Mosconi, E.; De Angelis, F. Mechanism of Reversible Trap Passivation by Molecular Oxygen in Lead-Halide Perovskites. *ACS Energy Lett.* **2017**, *2* (12), 2794–2798.

(27) Zheng, X.; Chen, B.; Dai, J.; Fang, Y.; Bai, Y.; Lin, Y.; Wei, H.; Zeng, X. C.; Huang, J. Defect Passivation in Hybrid Perovskite Solar Cells Using Quaternary Ammonium Halide Anions and Cations. *Nat. Energy* **2017**, *2* (7), 17102.

(28) Leijtens, T.; Eperon, G. E.; Barker, A. J.; Grancini, G.; Zhang, W.; Ball, J. M.; Kandada, A. R. S.; Snaith, H. J.; Petrozza, A. Carrier Trapping and Recombination: The Role of Defect Physics in Enhancing the Open Circuit Voltage of Metal Halide Perovskite Solar Cells. *Energy Environ. Sci.* **2016**, *9* (11), 3472–3481.

(29) Miyata, K.; Meggiolaro, D.; Trinh, M. T.; Joshi, P. P.; Mosconi, E.; Jones, S. C.; De Angelis, F.; Zhu, X.-Y. Large Polarons in Lead Halide Perovskites. *Sci. Adv.*

572 **2017**, *3* (8), e1701217.

573 (30) Tsai, H.; Asadpour, R.; Blancon, J.-C.; Stoumpos, C. C.; Durand, O.; Strzalka, J.
574 W.; Chen, B.; Verduzco, R.; Ajayan, P. M.; Tretiak, S.; Even, J.; Alam, M. A.;
575 Kanatzidis, M. G.; Nie, W.; Mohite, A. D. Light-Induced Lattice Expansion Leads
576 to High-Efficiency Perovskite Solar Cells. *Science (80-.).* **2018**, *360* (6384), 67–
577 70.

578 (31) Azpiroz, J. M.; Mosconi, E.; Bisquert, J.; De Angelis, F. Defect Migration in
579 Methylammonium Lead Iodide and Its Role in Perovskite Solar Cell Operation.
580 *Energy Environ. Sci.* **2015**, *8* (7), 2118–2127.

581 (32) Gottesman, R.; Haltzi, E.; Gouda, L.; Tirosh, S.; Bouhadana, Y.; Zaban, A.;
582 Mosconi, E.; De Angelis, F. Extremely Slow Photoconductivity Response of
583 $CH_3NH_3PbI_3$ Perovskites Suggesting Structural Changes under Working
584 Conditions. *J. Phys. Chem. Lett.* **2014**, *5* (15), 2662–2669.

585 (33) Barker, A. J.; Sadhanala, A.; Deschler, F.; Gandini, M.; Senanayak, S. P.; Pearce,
586 P. M.; Mosconi, E.; Pearson, A. J.; Wu, Y.; Srimath Kandada, A. R.; Leijtens, T.;
587 De Angelis, F.; Dutton, S. E.; Petrozza, A.; Friend, R. H. Defect-Assisted
588 Photoinduced Halide Segregation in Mixed-Halide Perovskite Thin Films. *ACS*
589 *Energy Lett.* **2017**, *2* (6), 1416–1424.

590 (34) Brennan, M. C.; Draguta, S.; Kamat, P. V.; Kuno, M. Light-Induced Anion Phase
591 Segregation in Mixed Halide Perovskites. *ACS Energy Lett.* **2018**, *3* (1), 204–213.

592 (35) Yoon, S. J.; Kuno, M.; Kamat, P. V. *Shift Happens* . How Halide Ion Defects
593 Influence Photoinduced Segregation in Mixed Halide Perovskites. *ACS Energy*
594 *Lett.* **2017**, *2* (7), 1507–1514.

595 (36) Eames, C.; Frost, J. M.; Barnes, P. R. F.; O'Regan, B. C.; Walsh, A.; Islam, M. S.
596 Ionic Transport in Hybrid Lead Iodide Perovskite Solar Cells. *Nat. Commun.* **2015**,

6, 7497.

(37) Meggiolaro, D.; Mosconi, E.; De Angelis, F. Modeling the Interaction of Molecular Iodine with MAPbI 3 : A Probe of Lead-Halide Perovskites Defect Chemistry. *ACS Energy Lett.* **2018**, *3* (2), 447–451.

(38) Boschloo, G.; Hagfeldt, A. Characteristics of the Iodide/Triiodide Redox Mediator in Dye-Sensitized Solar Cells. *Acc. Chem. Res.* **2009**, *42* (11), 1819–1826.

(39) Zhang, L.; Sit, P. H.-L. Ab Initio Study of the Role of Oxygen and Excess Electrons in the Degradation of CH 3 NH 3 PbI 3. *J. Mater. Chem. A* **2017**, *5* (19), 9042–9049.

(40) Wang, S.; Jiang, Y.; Juarez-Perez, E. J.; Ono, L. K.; Qi, Y. Accelerated Degradation of Methylammonium Lead Iodide Perovskites Induced by Exposure to Iodine Vapour. *Nat. Energy* **2016**, *2* (1), 16195.

(41) Sadoughi, G.; Starr, D. E.; Handick, E.; Stranks, S. D.; Gorgoi, M.; Wilks, R. G.; Bär, M.; Snaith, H. J. Observation and Mediation of the Presence of Metallic Lead in Organic–Inorganic Perovskite Films. *ACS Appl. Mater. Interfaces* **2015**, *7* (24), 13440–13444.

(42) Noel, N. K.; Abate, A.; Stranks, S. D.; Parrott, E. S.; Burlakov, V. M.; Goriely, A.; Snaith, H. J. Enhanced Photoluminescence and Solar Cell Performance via Lewis Base Passivation of Organic-Inorganic Lead Halide Perovskites. *ACS Nano* **2014**, *8* (10), 9815–9821.

(43) Ling, Y.; Tian, Y.; Wang, X.; Wang, J. C.; Knox, J. M.; Perez-Orive, F.; Du, Y.; Tan, L.; Hanson, K.; Ma, B.; Gao, H. Enhanced Optical and Electrical Properties of Polymer-Assisted All-Inorganic Perovskites for Light-Emitting Diodes. *Adv. Mater.* **2016**, *28* (40), 8983–8989.

(44) Wang, Z.; Luo, Z.; Zhao, C.; Guo, Q.; Wang, Y.; Wang, F.; Bian, X.; Alsaedi, A.;

Hayat, T.; Tan, Z. Efficient and Stable Pure Green All-Inorganic Perovskite CsPbBr3Light-Emitting Diodes with a Solution-Processed NiOxInterlayer. *J. Phys. Chem. C* **2017**, *121* (50), 28132–28138.

(45) Xu, J.; Buin, A.; Ip, A. H.; Li, W.; Voznyy, O.; Comin, R.; Yuan, M.; Jeon, S.; Ning, Z.; McDowell, J. J.; Kanjanaboos, P.; Sun, J.-P.; Lan, X.; Quan, L. N.; Kim, D. H.; Hill, I. G.; Maksymovych, P.; Sargent, E. H. Perovskite–fullerene Hybrid Materials Suppress Hysteresis in Planar Diodes. *Nat. Commun.* **2015**, *6* (1), 7081.

(46) Shao, Y.; Xiao, Z.; Bi, C.; Yuan, Y.; Huang, J. Origin and Elimination of Photocurrent Hysteresis by Fullerene Passivation in CH3NH3PbI3 Planar Heterojunction Solar Cells. *Nat. Commun.* **2014**, *5* (1), 5784.

SUPPLEMENTARY Info

Controlling competing photochemical reactions stabilises perovskite solar cells

Silvia G. Motti[1,2,5], Daniele Meggiolaro,[3,4] Alex J. Barker[1], Edoardo Mosconi,[4] Carlo Andrea Riccardo Perini[1,2], James M. Ball[1,5], Marina Gandini[1,2], Min Kim[1], Filippo De Angelis,[3,4,6*] Annamaria Petrozza[1*]

[1]Center for Nano Science and Technology @Polimi, Istituto Italiano di Tecnologia, via Giovanni Pascoli 70/3, 20133 Milan, Italy.

[2]Dipartimento di Fisica, Politecnico di Milano, Piazza L. da Vinci, 32, 20133 Milano, Italy.

[3]Computational Laboratory for Hybrid/Organic Photovoltaics (CLHYO), CNR-ISTM, Via Elce di Sotto 8, 06123, Perugia, Italy.

[4] D3-CompuNet, Istituto Italiano di Tecnologia, Via Morego 30, 16163 Genova, Italy.

[5]Current address: Department of Physics, University of Oxford, Clarendon Laboratory, Parks Road, Oxford, OX1 3PU, United Kingdom

[6]Dipartimento di Chimica, Biologia e Biotecnologie, Università di Perugia, Via Elce di Sotto 8, I-06123 Perugia, Italy.

*Annamaria.petrozza@iit.it; filippo@thch.unipg.it

Supplementary Information

Sample preparation

Lead(II) bromide ($PbBr_2$, ≥98%), N,N-dimethylformamide (DMF, anhydrous, 99.8%), Chlorobenzene (anhydrous, 99.8%), and dimethyl sulfoxide (DMSO, anhydrous, ≥99.9%) were purchased from Sigma-Aldrich; methylammonium bromide (MABr) and methylammonium iodide (MAI) were purchased from Dyesol; and lead (II) iodide (PbI_2, 99.9985%, CAS No. 10101-63-0) was purchased from Alfa Aesar. All chemicals were used without any further purification. Glass substrates were cleaned in acetone and isopropyl alcohol (IPA) for 10 minutes by sonication. The cleaned glass substrates were treated with Oxygen plasma for 10 minutes before any further deposition.

MAPbBr3 thin films. These films could be fabricated by an adapted Nanocrystal-Pinning technique [Ref. Cho H. et al., Science (2015), 350-6265, 1222-5]. In this case, two steps of spin-coating speed were used (500 rpm for 7 seconds, 3000 rpm 90 seconds). After spin-speed acceleration, a solution of MABr and PbBr2 (molar ratio 1.05:1) in DMSO was spin-coated onto the clean glass substrate. After 60 seconds, the pinning occurred by dropping 300 µl of chlorobenzene on the spinning sample. The samples were then baked at 90°C for 10 minutes.

$MAPbI_3$ thin films. These films were fabricated by quenching a precursor solution with an antisolvent during spin coating [M. Xiao et al., Angewandte Chemie vol. 126, p10056 (2014)], in a nitrogen filled glovebox. A 1.45 M precursor solution of PbI_2:MAI:DMSO in a molar ratio of 1:1:1 was prepared in DMF. This solution was spin coated onto the glass substrate at 4000 rpm, with an acceleration of 4000 rpm/s, for 15 s. After 6 s toluene, an antisolvent to the precursor solution, was dropped onto spinning sample by pipette. The samples were then annealed at 100°C for 10 minutes.

$MAPbI_3$ thin films with passivation.

tri-n-octylphosphine oxide (TOPO) or polyethylene oxide (PEO) were dissolved in anhydrous chlorobenzene at concentration of 10 $mg \cdot ml^{-1}$. Solutions were sonicated for 10 minutes for complete dissolution before deposition on top of the perovskite film by spin-coating at 4000 rpm.

705 **Device fabrication**

706 *Film fabrication*: ITO on glass substrate was etched with 2M aqueous HCl solution
707 and zinc powder (Sigma Aldrich). The ITO substrates were sequentially washed with 2%
708 Hellamanex in deionized water, deionized water, iso-propanol, acetone, iso-propanol in
709 a sonication bath, followed by O_2 plasma cleaning for 10 min. A cleaned ITO substrate
710 was covered with a SnO_2 layer (~20 nm) by spin-coating of a diluted SnO_2 nanoparticle
711 solution (Alfa Aesar) and annealed at 180 °C for 1 h. On the SnO_2 layer, C_{60} layer was
712 deposited from a C_{60} solution (10 mg·ml^{-1}) in 1,2-dichlorobenzene by spin-coating at
713 3000 rpm, followed by thermal annealing at 100 °C for 10 min. The perovskite layer was
714 fabricated through applying anti-solvent quenching method. For hole transport layer, a
715 spiro-MeOTAD solution was spin coated on the perovskite layer at 4000 rpm for 30 s.
716 Spiro-MeOTAD solution was prepared by dissolving 73 mg of spiro-MeOTAD in 1 mL
717 chlorobenzene (99.8%; Sigma–Aldrich), to which were added 28.8 μL of 4-tert-
718 butylpyridine (96%, Sigma-Aldrich), 17.5 μL lithium bis(trifluoromethanesulfonyl)imide
719 (LiTFSI) solution (520 mg LiTSFI in 1 mL acetonitrile, 99.8%, Sigma-Aldrich). This
720 fabrication process was carried out under controlled conditions in a glove-box
721 atmosphere. Finally, 75 nm gold was thermally evaporated on top of the device at a
722 pressure of 1×10^{-6} mbar to form the top-contact electrode.

723 **Photovoltaic characterization:**

724 All devices were measured under simulated AM1.5 solar illumination using a class
725 AAA solar simulator (Oriel Sol3A, Newport). The illumination intensity was calibrated
726 using an unfiltered certified Si reference diode (area = 4 cm^2, Newport) to be 100 mW/cm^2
727 (typical spectral mismatch factor of 1.01 for solar cells based on $CH_3NH_3PbI_3$). The
728 current density-voltage (J-V) characteristics were recorded with a Keithley 2440. No light
729 soaking or pre-biasing was applied before the J-V measurements. The illuminated
730 electrode area, defined with a holed black anodized aluminium mask, was 0.0935 cm^2.
731 Devices were measured in the ambient atmosphere at 23 ± 2°C and 40-60% relative
732 humidity. The scan rates of J-V sweep were 0.2 V s^{-1}. The forward scan started from 0 V
733 (the short circuit condition) to 1.4 V, while backward scan from 1.4 V to 0 V. The stability
734 of the current/power output with time was recorded for 120 s. The EQE was measured
735 with a home-built setup. EQE spectra were recorded using the monochromated (Bentham)
736 output from a tungsten halogen lamp calibrated with a Newport UV-818 photodiode.
737

Transient open circuit voltage measurements

The excitation source was a simulated AM1.5 solar illumination using a class AAA solar simulator (Oriel Sol3A, Newport) or an unfocused beam of a 450 nm CW diode laser (Oxxius). The beam was expanded to match the active area of device, ~0.1 cm^2, and the excitation power density were around 100 mW cm^{-2}. The devices were encapsulated using epoxy and glass, and then were mounted perpendicular to the excitation. Keythley 2401 was used to measure the transient open circuit voltage over a duration of time, ~1500 s.

Modulation frequency dependent Photoluminescence

Excitation was provided with a continuous wave (CW) diode laser (Oxxius laserboxx). The excitation wavelength was 405 nm for $MAPbBr_3$ films and 450 nm for $MAPbI_3$. Modulation was accomplished by a waveform generator connected directly to the laser. Pulse widths were kept fixed to exclude the effects of varying illumination times so we could probe only the dependence on the intervals in the dark. $MAPbI_3$ films were illuminated with pulses of 200 ns at frequencies of 1 kHz, 3 kHz, 10 kHz, and 30 kHz. $MAPbBr_3$ films were illuminated with pulses of 10 µs and frequencies of 50 Hz, 500 Hz and 5 kHz. Excitation fluences used were around 0.5 µJcm^{-2}, corresponding to an excitation density of ~10^{16} cm^{-3}. Samples were mounted inside a vacuum chamber mounted on a translation stage that allowed fresh spots to be probed between every curve by changing the sample height without damaging the collection alignment. PL was collected in reflection mode and focused into a fiber coupled to a spectrometer (Ocean Optics Maya Pro 2000).

Temperature dependent Photoluminescence

Excitation was provided with a CW diode laser (Oxxius laserboxx). The excitation wavelength was 405 nm for $MAPbBr_3$ films and 450 nm for $MAPbI_3$. Excitation intensity was around 50 mW/cm^2, corresponding to an estimated excitation density ~10^{16} cm^{-3}. Films were mounted in vacuum in a cold finger cryostat cooled with liquid N_2 (Oxford Instruments) perpendicular to the excitation line. The excitation beam was

directed to the sample by a dichroic mirror and PL was collected in reflection mode and focused into a fiber coupled to a spectrometer (Ocean Optics Maya Pro 2000).

Double sided illumination

The beam of a 560 nm CW diode laser (Oxxius) was expanded and collimated with a telescope to a diameter of ~3 mm. A beam splitter was used to obtain the two excitation lines and attenuators were used to balance the intensities. Samples were mounted inside a vacuum chamber (pressure below 10^{-5} mbar) and PL was collected at a right angle from the excitation line (Figure S1) and focused into a fiber coupled to a spectrometer (Ocean Optics Maya Pro 2000).

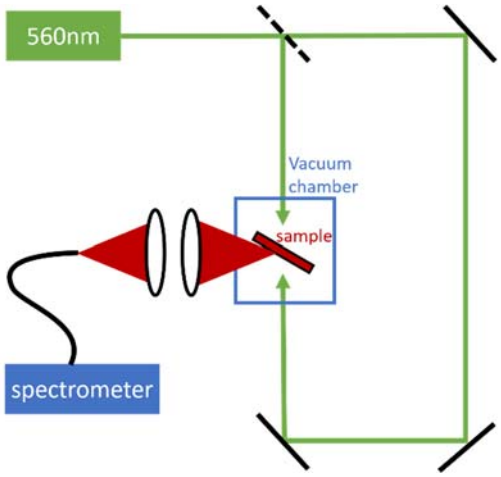

Figure S1. Schematics of the experimental setup used for double side illumination on thin films.

Photoluminescence on passivated samples

The excitation source was an unfocused beam of a 560 nm CW diode laser (Oxxius). Samples were mounted inside a vacuum chamber (pressure below 10^{-5} mbar) and PL was collected in reflection mode at a right angle from the excitation line and focused into a fiber coupled to a spectrometer (Ocean Optics Maya Pro 2000). Integrated PL over time was measured on fresh spots of the film with intensity ~40 mW/cm^2.

For relative PLQY measurements, the integrated PL was measured at varying excitation intensities and plotted as:

$$Relative\ PLQY = \frac{I_{PL}}{I_{pump}}$$

Excitation wavelength dependence

The excitation source was a supercontinuum laser (SuperK Extreme, NKT Photonics), which is spectrally filtered by an acousto-optic modulator (SuperK Select, NKT Photonics). The selected output is directed to a home-built transmission microscope in a confocal configuration. The sample is placed on top of a piezoelectric translation stage. The PL transients (Figure 2a) were taken tuning the wavelength of the acousto-optic modulator output a nd monitoring the PL over time with a spectrometer (Ocean Optics Maya Pro 2000) coupled to the microscope for detection.

Simulation of PL variations over time

A system of rate equations based on the model proposed by Stranks et al.[1] was used to simulate the evolution of the populations of free electrons, free holes and trapped carriers (Figure S2-S4). The model considers one single type of trap, assuming that in the presence of both hole and electron traps the more abundant type dominates the dynamics. In our case we consider the electron traps as dominant leading to the following system of equations:

$$\frac{dn_e}{dt} = G - \beta_{rad} n_e n_h - k_t n_e (N_t - n_t) - \gamma n_e n_h^2$$

$$\frac{dn_h}{dt} = G - \beta_{rad} n_e n_h - R_t n_h n_t - \gamma n_e n_h^2$$

$$\frac{dn_t}{dt} = k_t n_e (N_t - n_t) - R_t n_h n_t$$

where n_e is the density of free electrons, n_h is the density of free holes, n_t is the density of trapped carriers, G is the photogeneration rate, β_{rad} is the radiative recombination rate, γ is the Auger recombination rate, k_t is the trapping rate, N_t is the density of available traps, and R_t is the rate of recombination of a trapped electrons with free holes.

The PL intensity at a given time is

$$I_{PL} = \beta_{rad} n_e n_h$$

The parameters used in our simulations for modulated illumination were:

$$\beta_{rad} = 5 \cdot 10^{-10}\ cm^3/s$$
$$k_t = 1 \cdot 10^{-10}\ cm^3/s$$
$$R_t = 1 \cdot 10^{-12}\ cm^3/s$$
$$\gamma = 1 \cdot 10^{-26}\ cm^3/s$$
$$N_t = 1 \cdot 10^{16}\ cm^{-3}$$

These values were chosen based on fits of experimental data, including the low rate for trapped carrier recombination, which is consistent with a fit of hole dynamics (Figure S2) to our previous results from transient absorption measurements[2,3].

We obtain the evolution of the carrier populations in time switching the generation rate on and off to simulate the modulated illumination. The PL intensity can change over time because of pulse piling up and trap filling effects, but in the conditions similar to the experiments performed in this work, these effects should reach a steady state condition on a scale shorter than milliseconds. Several variations of the parameters above were tested in order to rule out that longer timescales could result from different combinations of values, but in all the possible scenarios we considered, stable PL is established after no more than a second. In the section below we discuss the results of these simulations in the interpretation of our experimental observations.

Role of electronic effects in PL dynamics in Fig 1 of the Manuscript

We can exclude the role of pure electronic processes, i.e. trap filling effects, on the observed PL dynamics in the milliseconds/seconds time domain. This can be visualized by the simulations reported in Figure S22-25. The simulations have been performed as described in the section "Simulation of PL variations over time" above. Here the simulations are run by testing up to 500 pulses coming at different frequencies between 1 kHz and 30 kHz. For each defined frequency we plot the electron and hole dynamics, the trap sites filling and the corresponding PL dynamics. It is clear that even when trap state filling start piling up, above 10 kHz, the PL reach a steady state condition well before the ms-s time regime, where we probe the PL quenching and enhancement transients. Moreover, it is worth noticing that increasing the pulse frequency mainly leads to pile up effects, i.e. growing population upon trap filling and this should lead to an enhancement of the PL, while we observe the PL quenching kicking in.

The main effect correlated to an enhancement of the average flux density is an enhancement of the PL absolute value at time t=0, due to an associated enhancement of counts during the integration (see Figure S26).

Frequency	δ (time between pulses)	Pulse energy	Average Intensity
1 kHz	1 ms	0.2 nJ	0.6 mW/cm^2
3 kHz	0.33 ms	0.2 nJ	2 mW/cm^2
10 kHz	0.1 ms	0.2 nJ	6 mW/cm^2
30 kHz	0.033 ms	0.2 nJ	20 mW/cm^2

Table S2. Average intensity as a function of the change in the excitation repetition rate.

Computational details

All calculation have been carried out with Quantum Espresso[4] program package.

Defects formation energies and ionization levels calculations:

DFT calculations have been performed in the tetragonal phases of $MAPbI_3$ and $MAPbBr_3$. In all cases the cell parameters have been fixed to the experimental values, i.e. a=b=8.849 Ang, c = 12.642 Å for $MAPbI_3$[5]; a=b=8.345, c = 11.802 Å for $MAPbBr_3$.

Defects structures have been calculated in the 2x2x1 supercells for both $MAPbI_3$ and $MAPbBr_3$ by using the PBE functional[6] and ultrasoft pseudopotentials with a cutoff on the wavefunctions of 40 Ryd (320 Ryd on the charge density) and 1x1x2 k-point grids in the Brillouin zone (BZ). Defects calculations have been thus refined at the hybrid level by using the HSE06 functional[7] (α=0.43) by including spin-orbit corrections and dispersions interactions a posteriori within the DFT-D3 scheme.[8] Single point hybrid calculations have been performed at the calculated PBE structures by using norm conserving pseudopotentials and a cutoff energy on the wavefunctions of 40 Ryd and 1x1x2 k-points in the BZ.

Defects formation energies and thermodynamic ionization levels have been calculated following the approach reported in Ref.[9] Chemical potentials have been set by imposing thermodynamic equilibrium between perovskites and the relative lead precursors, i.e.

$$\mu(MAPbI_3)=\mu(MA)+ \mu(Pb) + 3\mu(I) , \quad \mu(Pb) + 2\mu(I) = \mu(PbI_2)$$

$$\mu(MAPbBr_3)=\mu(MA)+ \mu(Pb) + 3\mu(Br) , \quad \mu(Pb) + 2\mu(Br) = \mu(PbBr_2)$$

Halides medium conditions have been modelled by using intermediate chemical potentials between halide-rich and halide-poor conditions. For halide rich conditions I and Br chemical potentials have been fixed to the values of the respective gas molecules, i.e. $\mu(I) = ½ \mu(I_2^{gas})$ and $\mu(Br) = ½ \mu(Br_2^{gas})$, while in halide poor conditions the chemical potentials of lead has been set to the metallic bulk Pb. Defects formation energies have been corrected by including potential alignment and Makov-Payne corrections[10] (ionic dielectric constants ε=24.0 and ε=20.0 for $MAPbI_3$ and $MAPbBr_3$, respectively).

2x2x2 Supercell and slabs calculations

Geometry optimizations are carried out at Γ point using experimental cell parameters along with plane-wave basis set cutoffs for the smooth part of the wave functions and augmented electronic density expansions of 25 and 200Ry, respectively. Electrons-ions interactions were described by ultrasoft pseudo-potentials with electrons from I 5s, 5p; N, C 2s, 2p; O 2s 2p; H 1s; Pb, 6s, 6p, 5d; shells explicitly included in calculations. For the slab simulation we take into account both the 001 MAI- and PbI_2-terminated surface with a thickness of three and five Pb layers, respectively. A 10 Å of vacuum was added along the c non periodic direction.

Car-Parrinello Molecular Dynamics

Car-Parrinello Molecular Dynamics[11,12] have been carried out using a 2x2x2 supercell $MAPbI_3$ model generated by duplicating the 1x1x1 optimized structure using the experimental cell parameters. Electrons-ions interactions were described by ultrasoft pseudo-potentials with electrons from I 5s, 5p; N, C 2s, 2p; H 1s; Pb 6s, 6p, 5d; shells explicitly included in calculations. Plane-wave basis set cutoffs for the smooth part of the wave functions and augmented electronic density expansions of 25 and 200Ry, respectively. A time step of 10 a. u., electronic mass of 1000 a.u. and masses equal to 5.0 a.m.u have been used for all atoms. The simulation has been carried out at 400 K for a simulation time of 14 ps comprising the initial thermalization.

913

914 **I2 production under illumination**

915 We have identified hexane as a good solvent for I2 and poor solvent for PEO, allowing
916 us to investigate I2 formation free of other solvent induced degradation processes.

917 We prepared three thin films, a pristine MAPbI3, and two twin samples coated by
918 PEO and polystyrene (PS), respectively. The use of PS serves as blank, as this system
919 covers the perovskite surface without significant chemical interaction (Energy Environ.
920 Sci., 2018, 11, 2609-2619) thus representing a simple capping agent.

921 In figure S18 we show the I_2 absorption spectrum in hexane, characterized by a broad
922 band peaking at about 520 nm.[14]

923 We kept the uncoated, PS- and PEO-coated samples under illumination for 36h in a
924 vial full of hexane and during this time window we monitored the absorption spectrum of
925 the ensuing solution, Figure R4a-c. In line with results by Kim et al.[15], we see that under
926 photo-excitation I_2 molecules reach the perovskite surface and are then dissolved in the
927 solvent, as demonstrated by the growing 520nm band over time . Importantly, in the
928 presence of the inert PS coating, the concentration of I_2 in the hexane solution is the same
929 as the one produced by the uncoated thin film. On the other hand, the presence of PEO
930 strongly reduces the I2 production. This can be clearly visualized Figure S19 where we
931 show the integrated area of the band at 520nm versus time. Notably, leaving the three
932 twin samples in contact with a hexane solution in the dark, as a control experiment, no
933 trace of I_2 could be probed for either uncoated, PS- and PEO-coated samples (Fig S19).

934 This set of observations represent an experimental evidence of our model,
935 demonstrating that chemically active surface passivation, not simple coating, provides a
936 mean to reduce I2 loss from the perovskite thin film under photo-excitation, pointing at
937 the surface as the preferential site for defect nucleation and formation.

938 It is also worth to notice that a small amount of I_2 is observed also in the PEO-coated
939 sample, which we tentatively ascribe to some degradation of the thin film coating over
940 time, as we observe through AFM analysis of the surface (Figure S20)

941

942 **PL temporal evolution in T and structural phase transition**

To further exclude any direct dependence form the crystalline phase, in Figure S27, we show the PL spectra of $MAPbI_3$, over time, at certain temperatures where the thin film is undergoing the phase transition, therefore one can observe at the same time the emission from the orthorhombic and tetragonal phases.[16,17] Both peaks showed a slight enhancement, in a similar way, demonstrating that the phenomenon is not related to the specific crystalline phases but rather to the specific thermal energy available.

On the computational side, DFT simulations of defects in $MAPbI_3$ and $MAPbBr_3$ have been carried out in the related tetragonal cells in order to obtain comparable defect formation energies and thermodynamic ionization levels of the two systems, by avoiding possible variation associated to the different band edges estimate of the tetragonal and cubic phases. Such variations may affect the calculation of defects formation energies and ionization levels.

Supplementary figures

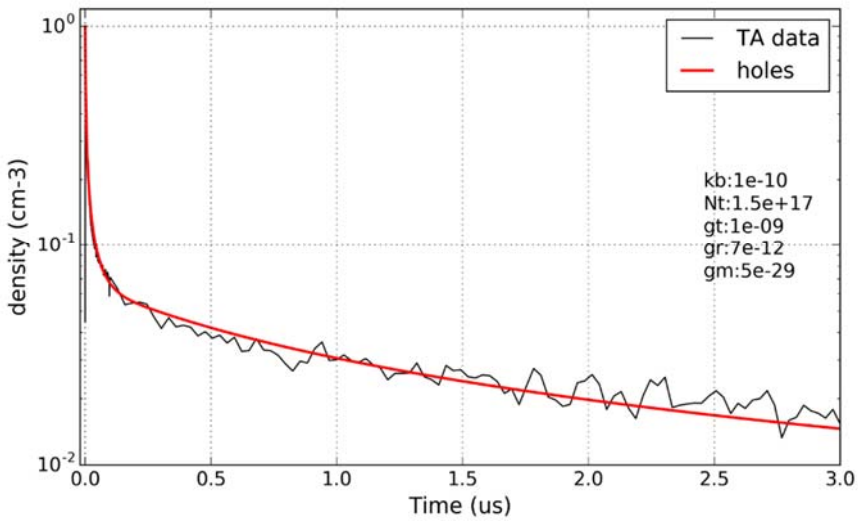

Figure S2. Transient Absorption at the band edge of a MAPbBr3 film (525nm) and a fit of the hole dynamics resulting from the rate equation model described.

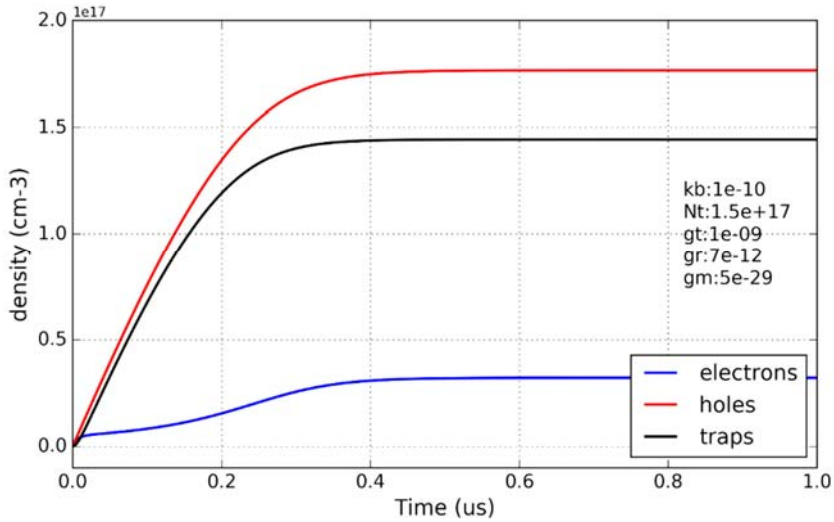

Figure S3. Simulation of the evolution of carrier populations in time under CW illumination until steady state conditions are reached.

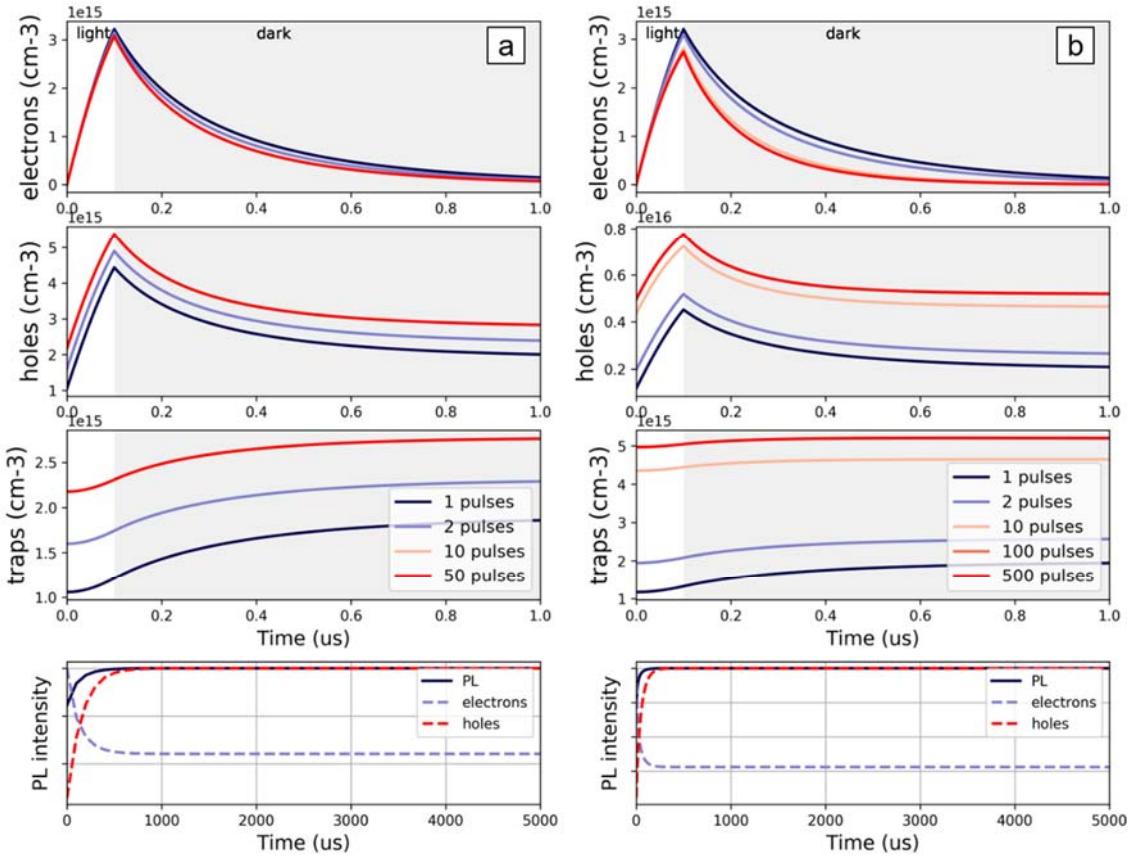

Figure S4. Simulation of the modulated illumination with pulses of 100ns and frequencies of (a) 10 kHz and (b) 100 kHz.

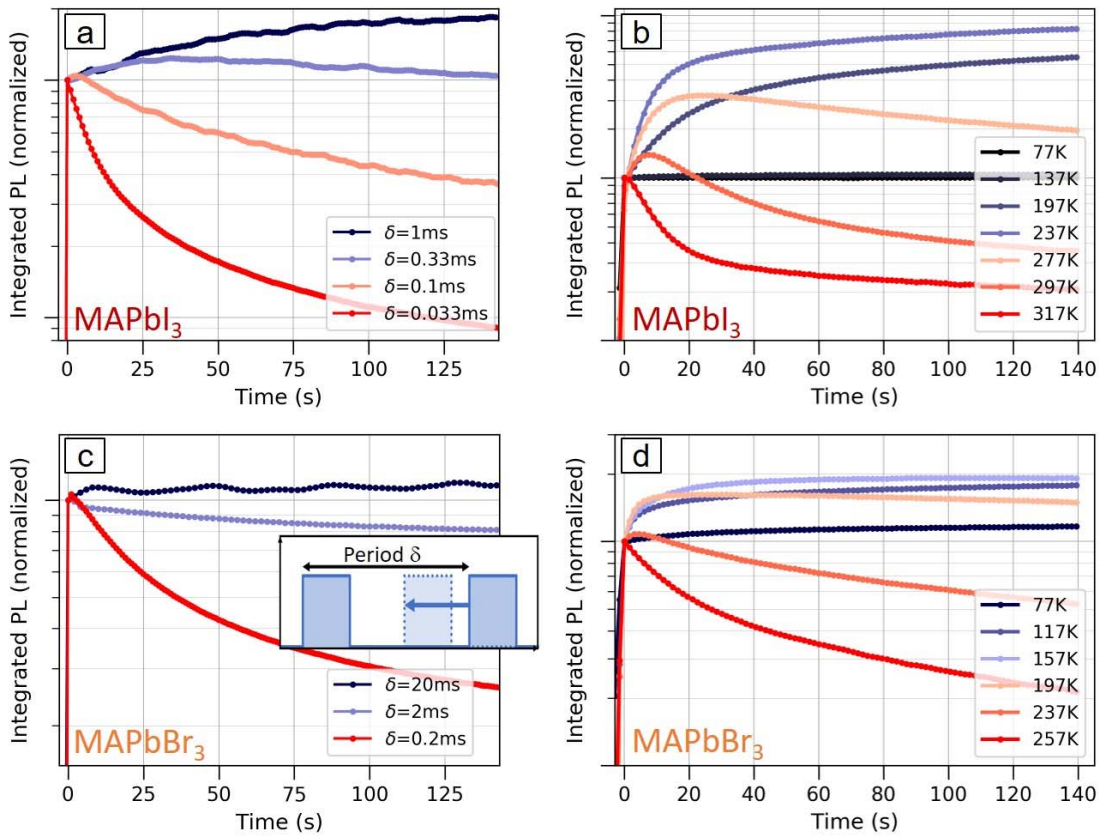

Figure S5. Reproduction of Fig 1 of the manuscript with the pulse width for $MAPbBr_3$ in c) fixed at 10 µs.

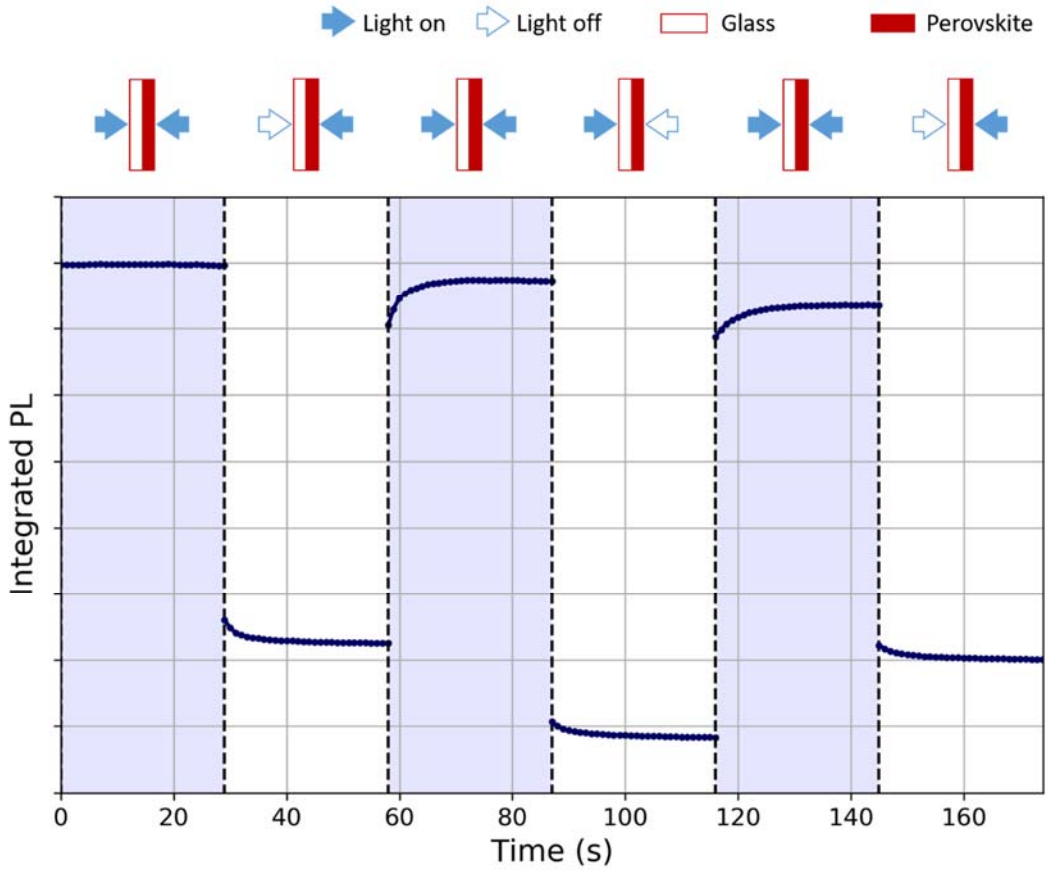

Figure S6. Integrated PL intensity over time of a $MAPbI_3$ film on glass. Excitation is performed with symmetrical beams of equal intensity (CW illumination, 560 nm) impinging on both the perovskite and glass side of the sample.

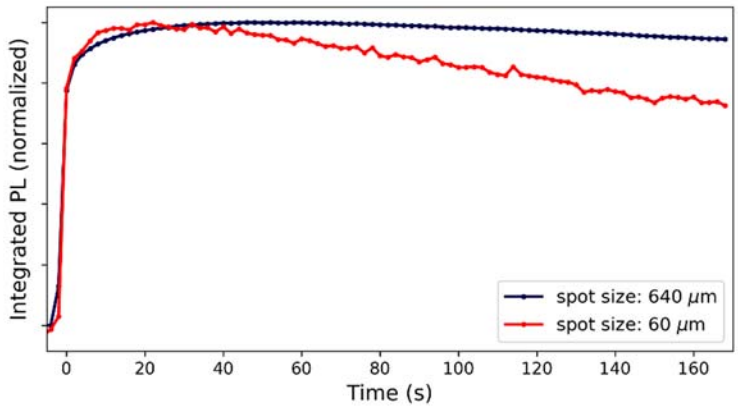

Figure S7. Normalized integrated PL over time of a $MAPbBr_3$ film obtained using a 450 nm CW diode laser focalized into 640 µm or 60 µm spot size, with fixed intensity of 21 mW/cm^2.

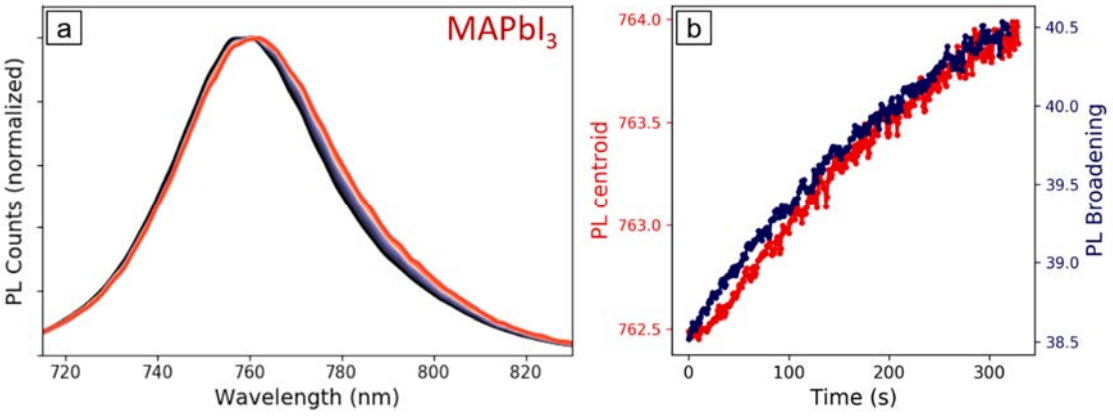

Figure S8. a) PL spectrum of a $MAPbI_3$ film in PLD conditions (100 kHz, 200 ns pulses), from t=0 s (dark blue) to t=300 s (red) under illumination, and b) PL broadening and shift of center of mass over time. When we monitor the spectrum of the emission during the PL quenching process, we see a small but consistent transformation to broader linewidths, consistent with a heating scenario. The PL position also slightly red shifts, which is the opposite behavior from the usual temperature dependence on this material.[13] We suggest these spectral changes result from the increase of traps in the film, increasing the disorder in the lattice and density of subgap states.

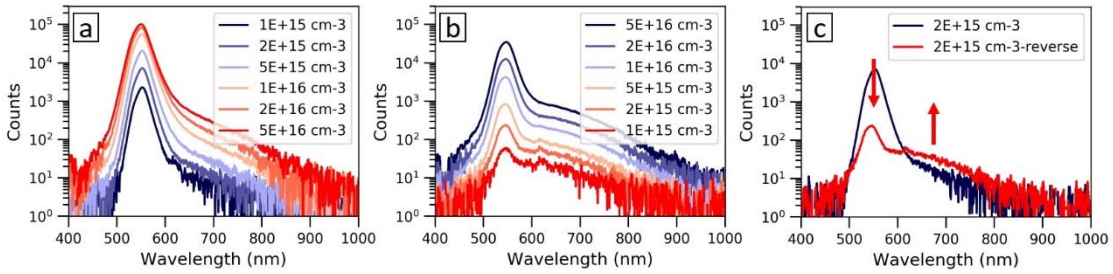

Figure S9. PL spectra of a $MAPbBr_3$ thin film with a) increasing and b) decreasing excitation intensity, and c) comparison of the PL spectra at a single excitation intensity before and after the intensity cycle.

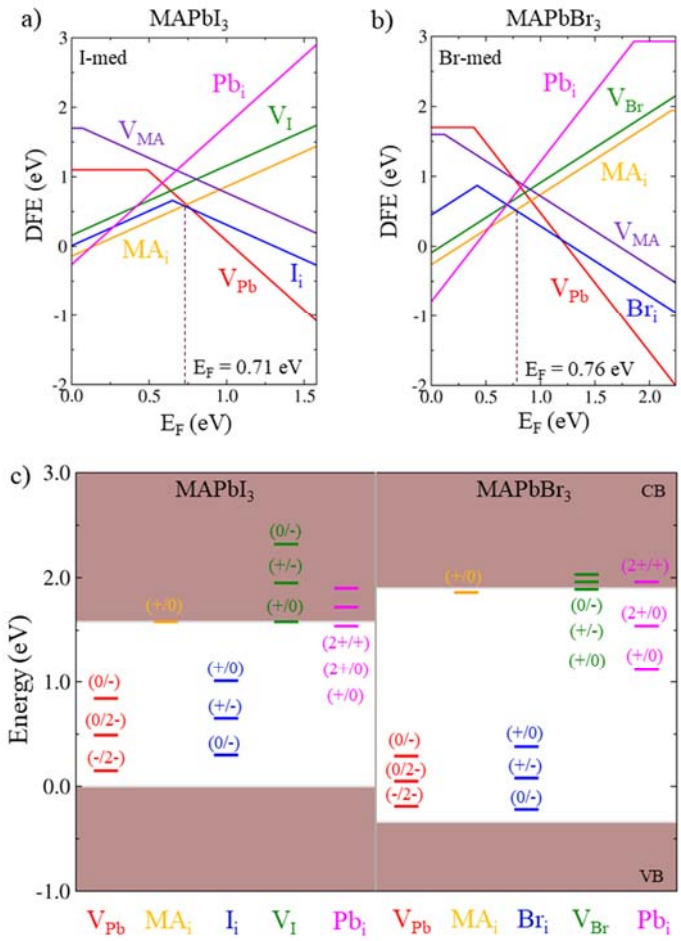

Figure S10. Defects formation energies of a) $MAPbI_3$ and b) $MAPbBr_3$ calculated in halide medium conditions by using the HSE06 functional (α=0.43) by including spin orbit coupling and a posteriori dispersion corrections; c) Associated thermodynamic ionization levels.

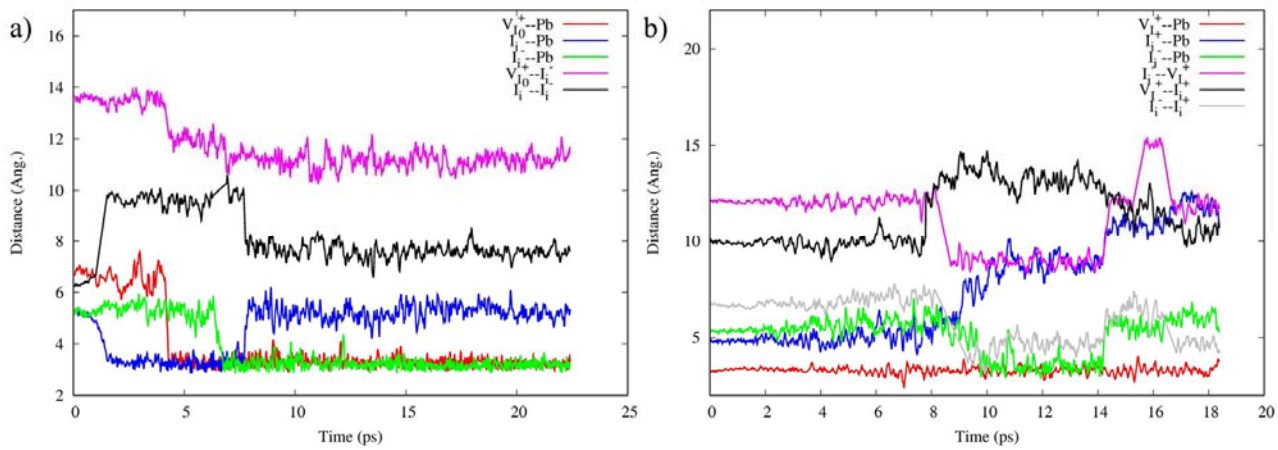

Figure S11. (a) Dynamical evolution of the system after electron trapping at I_i^+. A sequence of ion reorganization and migration events can be visualized: 1) following electron trapping at I_i^+, the system rapidly reaches the minimum energy structure of I_i^0 (blue curve) increasing the I_i^0/ I_i^- distance (black curve); 2) V_I^+ migrates in the direction of I_i^- (red and magenta lines); 3) I_i^- further migrates in the direction of V_I^+ (green and magenta lines). (b) Dynamical evolution of the system I_i^+/I_i^- in presence of a V_I^+. A sequence of ion reorganization and migration events can be visualized. In particular the migration of I_i^+ (blue) appears simultaneously with the migration of I_i^- (green), while the V_I^+ remain in its original position (red). The I_i^+/I_i^- migrates coupled and the defects separation is not found (gray) and it does not move towards to the V_I^+ (black).

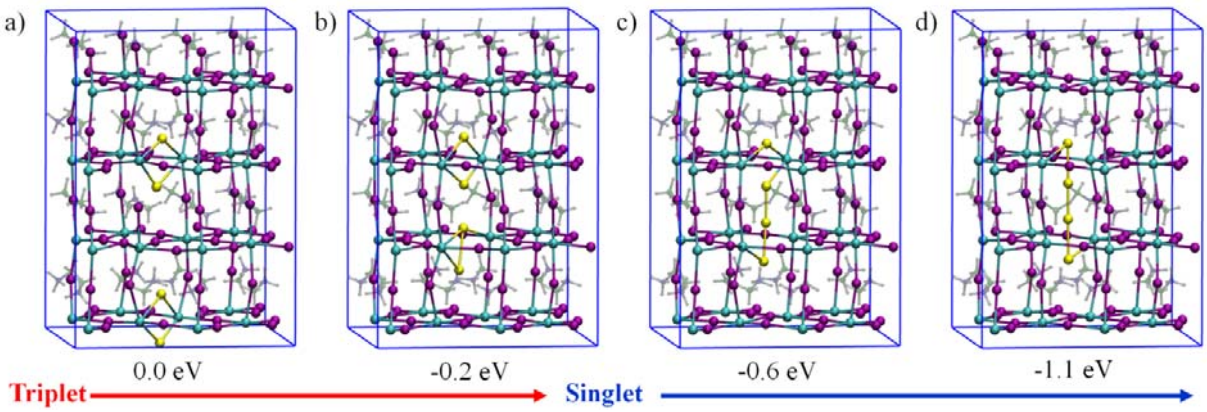

Figure S12. Radical quenching reaction of two I_i^0 species with associated energetics. The initial stage features a global triplet state corresponding to the two non interacting radicals. Upon shortening the inter-radical distance, a singlet state is stabilized by the

electron pairing to form the I-I bond. The system spontaneously evolves towards the formation of a coordinated I_2 molecule.

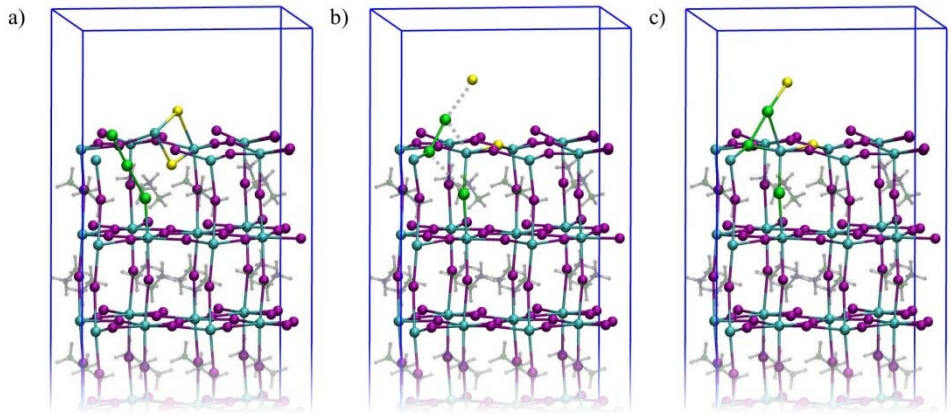

Figure S13. Direct I_i^-/I_i^+ (a) recombination to move through the transition state (b) towards to the final I_2 product (c). This is calculated on the (001) PbI_2-terminated surface with I_2 adsorbed (c). The transition state is calculated 0.33 eV above the reagent.

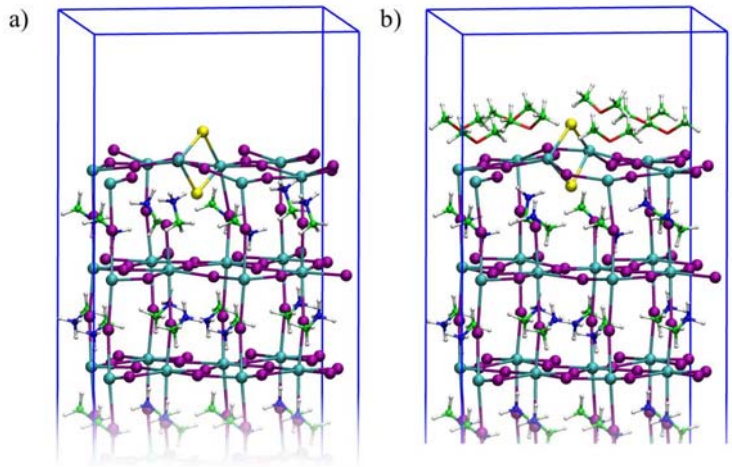

Figure S14. I_i^0 defect at the PbI_2-terminated surface bare (a) and with di-methyl ether (b). The formation energy of the I_i^0 defect in the presence of the di-methyl ether capping layer is less favorable by 0.1 eV with respect the bare surface.

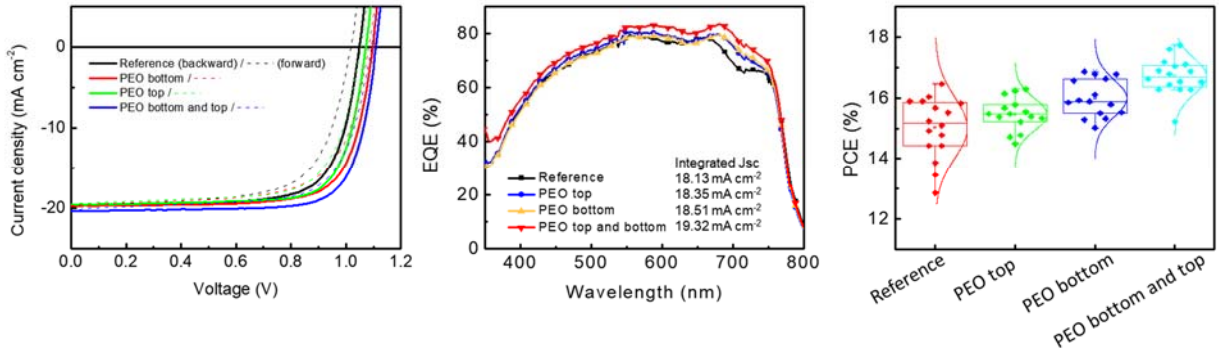

Figure S15. (a) Forward scan (dash lines) and backward scan (solid lines) J-V curves, (b) External quantum efficiency (EQE) spectra, and (c) Performance parameters (from 16 cells) of the perovskite devices with and without PEO passivation.

	Scan direction	J_{sc} (mA/cm^2)	V_{oc} (V)	PCE (%)	FF
Reference	Backward	19.72	1.049	15.05	0.73
	Forward	19.66	1.017	13.55	0.68
Bottom	Backward	19.70	1.097	16.14	0.75
	Forward	19.64	1.082	14.46	0.68
Top	Backward	19.57	1.071	15.86	0.76
	Forward	19.51	1.054	14.47	0.70
Bottom and top	Backward	20.35	1.109	17.23	0.76
	Forward	20.29	1.092	15.50	0.70

Table S1. Device parameters of the perovskite devices with and without PEO passivation.

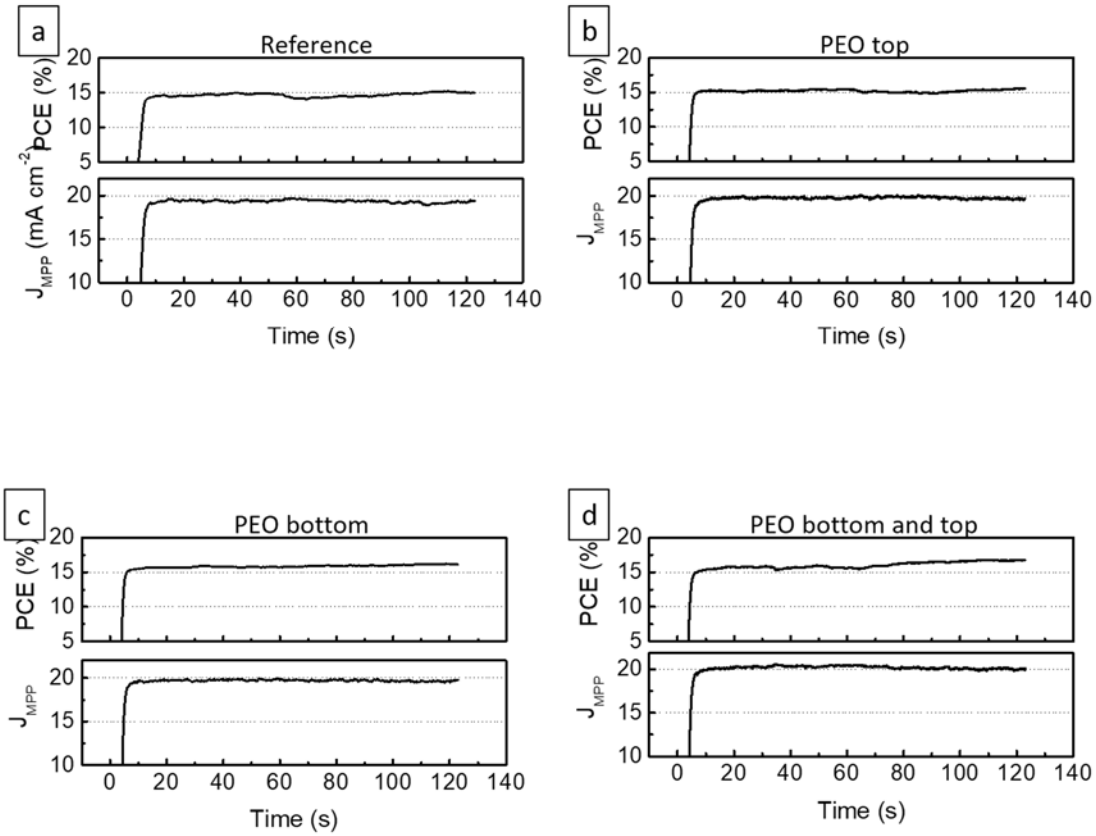

Figure S16. Time evolution of the maximum power point and with the photocurrent at maximum power point.

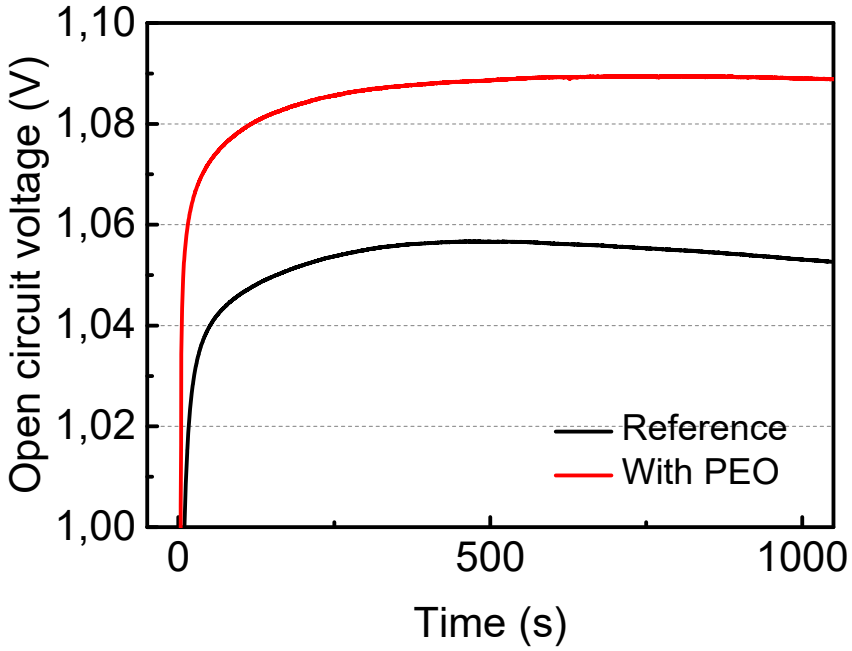

Figure S17. open-circuit voltage (Voc) transient measured from solar cells with and without PEO interlayers under an unfocused beam of a 450 nm CW diode laser (Oxxius).

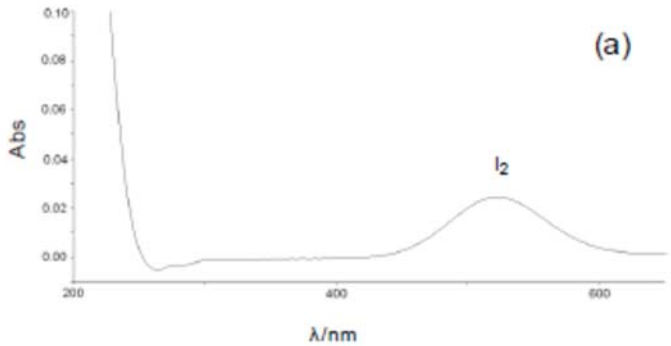

Figure S18. Absorption spectrum of I_2 in hexane, taken from Atmos. Meas. Tech., 3, 177–185, 2010.

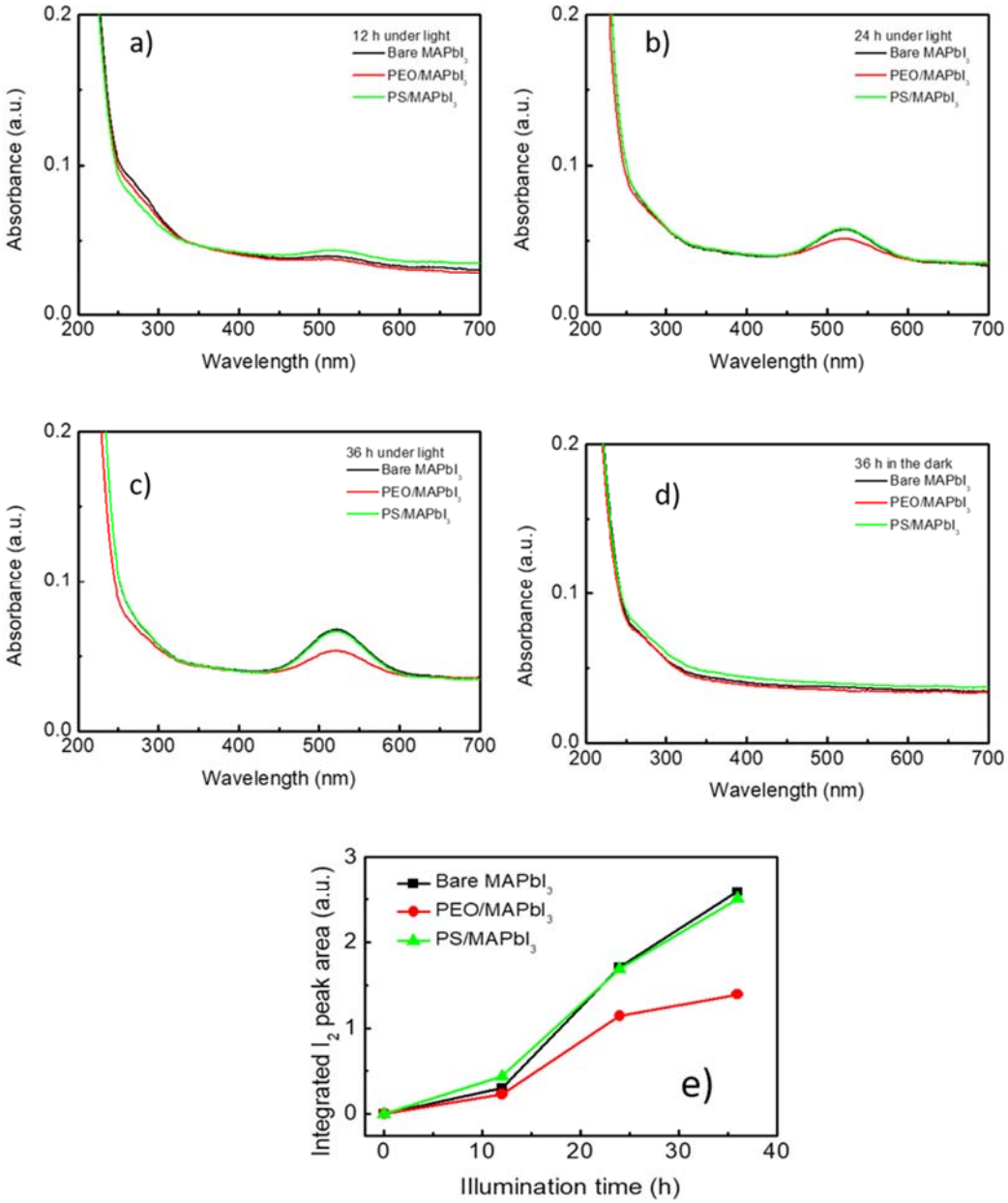

Figure S19. The absorption spectra of the hexane solution contained in the vials with uncoated, PS- and PEO-coated samples under illumination for a) 12h, b)24h, c) 36h and d) in dark for 36h. e) Integrated I2 peak area over time as measured in a)-c).

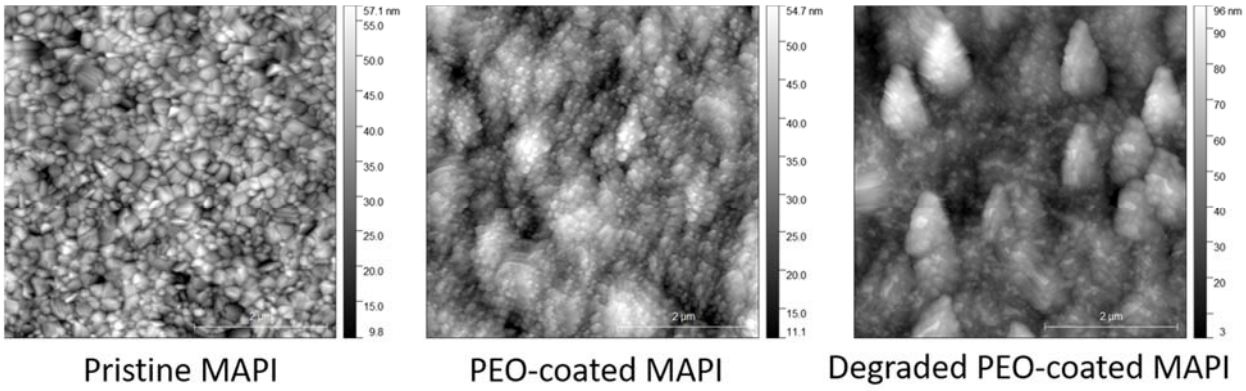

Figure S20. AFM top images of the bare and PEO-coated MAPbI3 thin films measured in Figure R4, showing the partial decomposition of the PEO layer by the hexane.

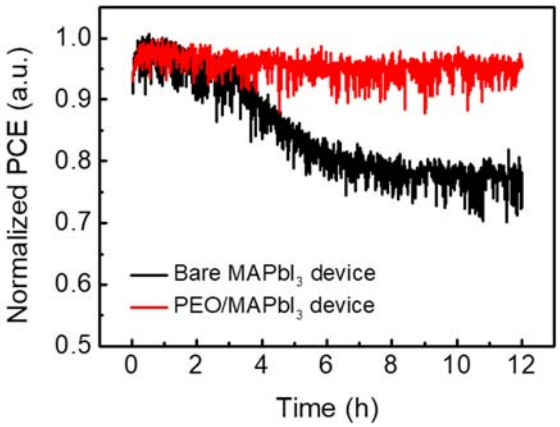

Figure S21. Solar cells based on bare $MAPbI_3$ and PEO sandwiched MAPbI3 tested at the maximum power point, under full solar spectrum illumination (1SUN). The devices were encapsulated to exclude environmental effects.

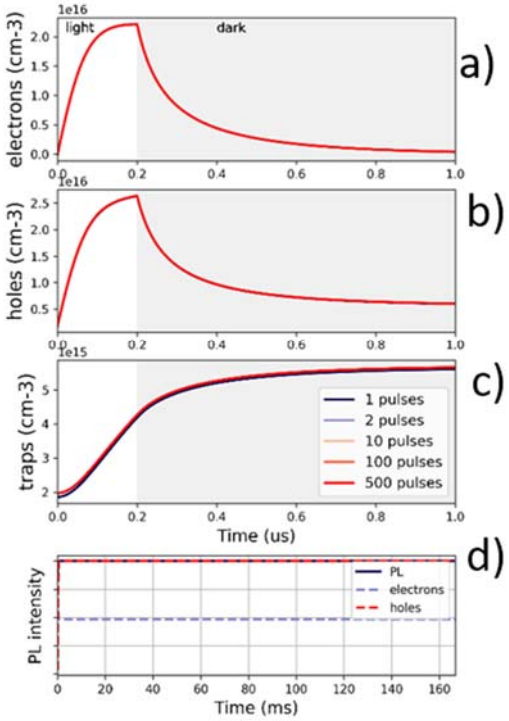

Figure S22. Simulation of a) electron, b) hole, c) trap population dynamics and d) the corresponding photoluminescence intensity over time for pulse length of 200 ns, pulse energy 0.2 nJ, repetition rate 1 kHz, average power 0.6 mW/cm^2.

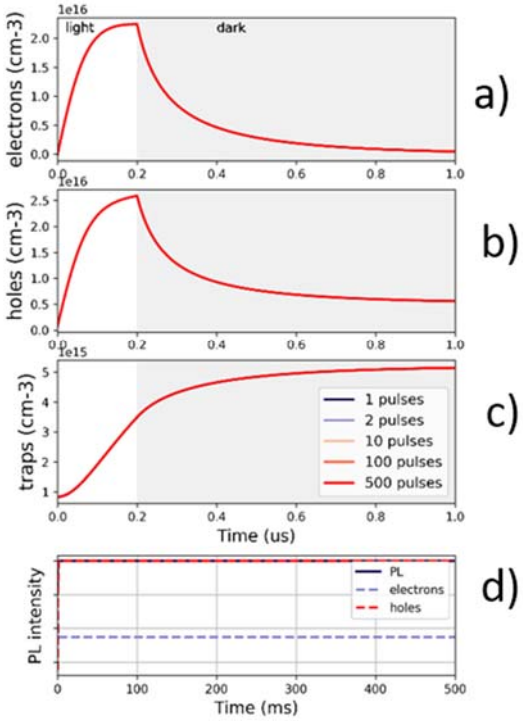

Figure 23. Simulation of a) electron, b) hole, c) trap population dynamics and d) the corresponding photoluminescence intensity over time for pulse length of 200 ns, pulse energy 0.2 nJ, repetition rate 3 kHz, average power 2 mW/cm^2.

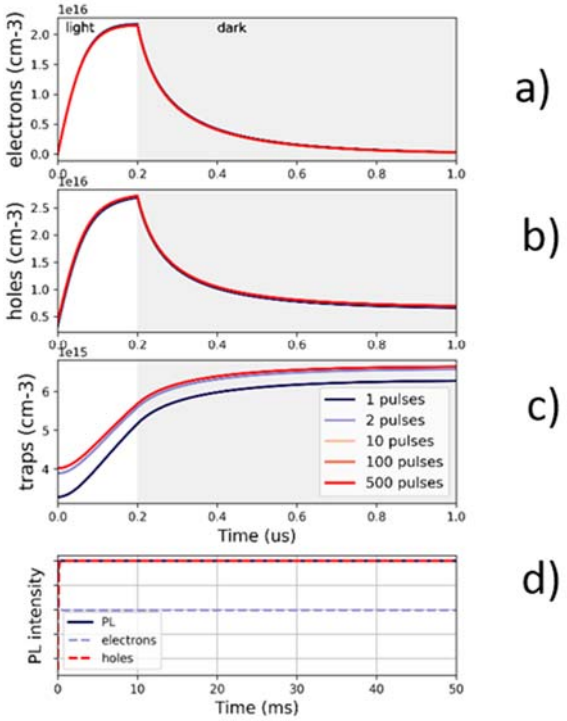

Figure S24. Simulation of a) electron, b) hole, c) trap population dynamics and d) the corresponding photoluminescence intensity over time for pulse length of 200 ns, pulse energy 0.2 nJ, repetition rate 10 kHz, average power 6 mW/cm^2.

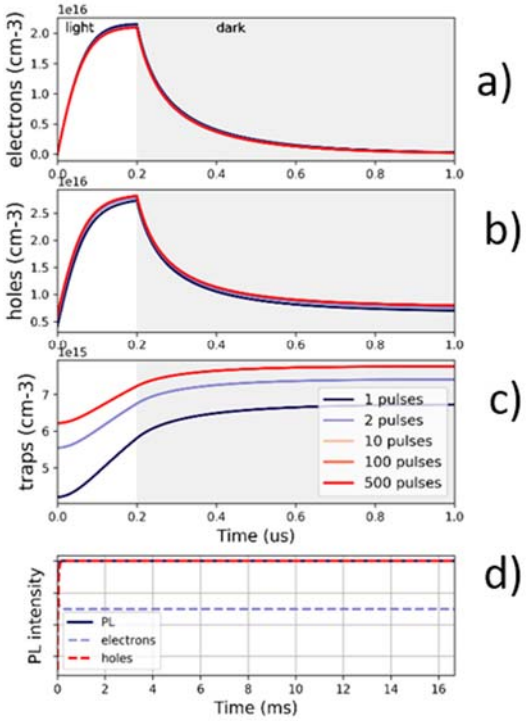

Figure S25. Simulation of a) electron, b) hole, c) trap population dynamics and d) the corresponding photoluminescence intensity over time for pulse length of 200 ns, pulse energy 0.2 nJ, repetition rate 30 kHz, average power 20 mW/cm^2.

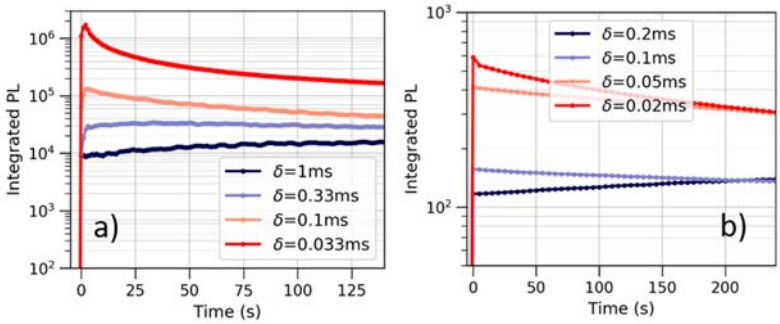

Figure S26. not normalized integrated PL dynamics at different repetition rates.

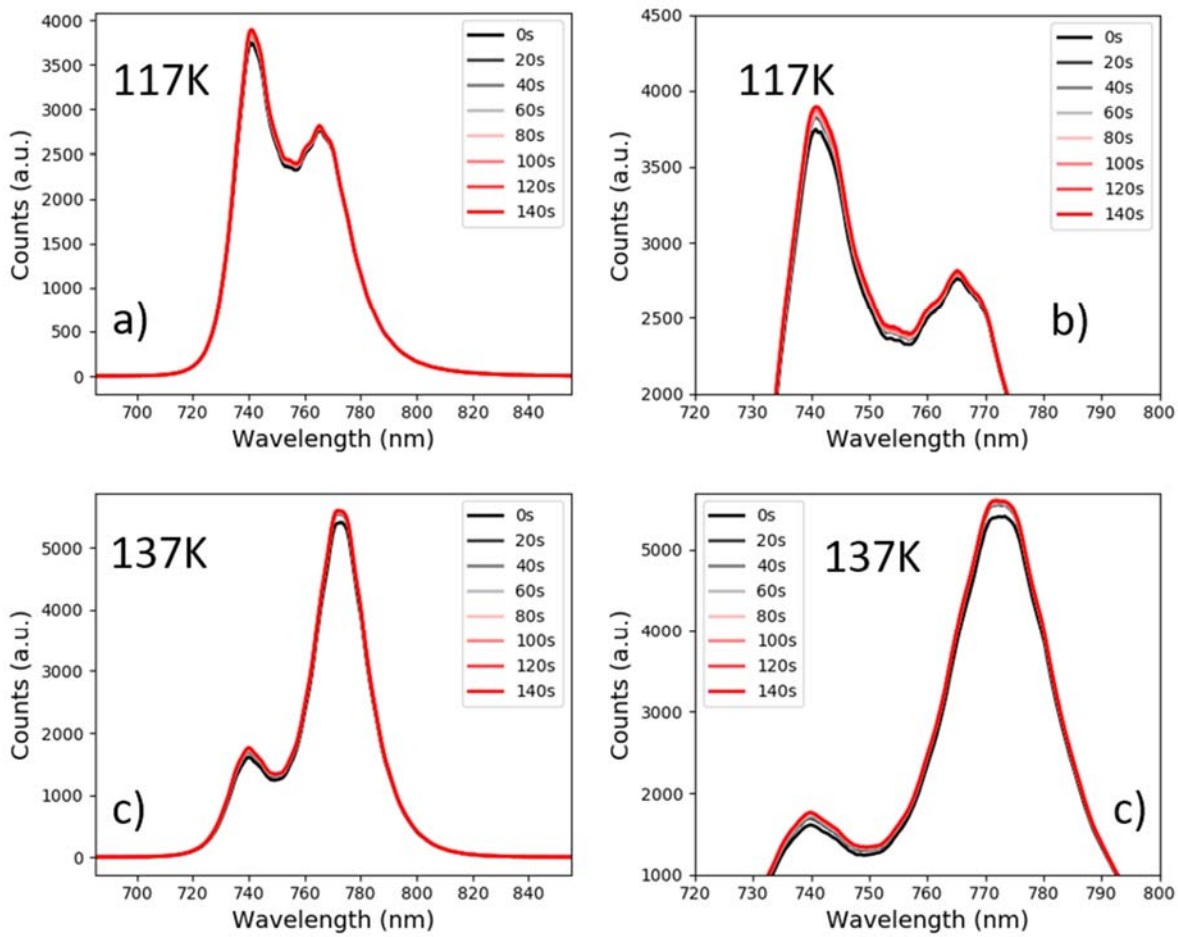

Figure S27. Temporal evolution of $MAPbI_3$ PL spectra at temperatures across the phase transitions. Figure b) and c) are a zoom in of the spectra in Fig a) and b).

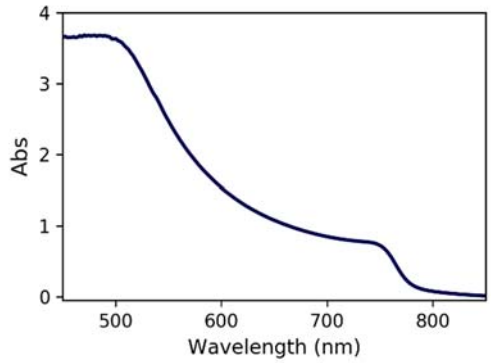

Figure R28. Absorption spectrum of $MAPbI_3$.

References:

1. Stranks, S. D. *et al.* Recombination Kinetics in Organic-Inorganic Perovskites: Excitons, Free Charge, and Subgap States. *Phys. Rev. Appl.* **2,** 034007 (2014).
2. Motti, S. G. *et al.* Photoinduced Emissive Trap States in Lead Halide Perovskite Semiconductors. *ACS Energy Lett.* **1,** 726–730 (2016).
3. Leijtens, T. *et al.* Carrier trapping and recombination: the role of defect physics in enhancing the open circuit voltage of metal halide perovskite solar cells. *Energy Environ. Sci.* **9,** 3472–3481 (2016).
4. Giannozzi, P. *et al.* QUANTUM ESPRESSO: A modular and open-source software project for quantum simulations of materials. *J. Phys. Condens. Matter* **21,** 395502 (2009).
5. Stoumpos, C. C., Malliakas, C. D. & Kanatzidis, M. G. Semiconducting tin and lead iodide perovskites with organic cations: Phase transitions, high mobilities, and near-infrared photoluminescent properties. *Inorg. Chem.* **52,** 9019–9038 (2013).
6. Perdew, J. P., Burke, K. & Ernzerhof, M. Generalized gradient approximation made simple. *Phys. Rev. Lett.* **77,** 3865–3868 (1996).
7. Heyd, J., Scuseria, G. E. & Ernzerhof, M. Hybrid functionals based on a screened Coulomb potential. *J. Chem. Phys.* **118,** 8207–8215 (2003).
8. Sitarz, M., Wirth-Dzieciolowska, E. & Demant, P. Loss of heterozygosity on chromosome 5 in vicinity of the telomere in γ-radiation-induced thymic lymphomas in mice. *Neoplasma* **47,** 148–150 (2000).
9. Van de Walle, C. G. & Neugebauer, J. First-principles calculations for defects and impurities: Applications to III-nitrides. *J. Appl. Phys.* **95,** 3851–3879 (2004).
10. Makov, G. & Payne, M. C. Periodic boundary conditions in ab initio calculations. *Phys. Rev. B* **51,** 4014–4022 (1995).
11. Car, R. & Parrinello, M. Unified approach for molecular dynamics and density-functional theory. *Phys. Rev. Lett.* **55,** 2471–2474 (1985).
12. Giannozzi, P., De Angelis, F. & Car, R. First-principle molecular dynamics with ultrasoft pseudopotentials: Parallel implementation and application to extended

bioinorganic systems. *Journal of Chemical Physics* **120,** 5903–5915 (2004).

13. D'Innocenzo, V. *et al.* Excitons versus free charges in organo-lead tri-halide perovskites. *Nat. Commun.* **5,** 3586 (2014).
14. Chance, R. J., Shaw, M., Telgmann, L., Baxter, M. & Carpenter, L. J. A comparison of spectrophotometric and denuder based approaches for the determination of gaseous molecular iodine. *Atmos. Meas. Tech.* **3,** 177–185 (2010).
15. Kim, G. Y. *et al.* Large tunable photoeffect on ion conduction in halide perovskites and implications for photodecomposition. *Nat. Mater.* **17,** 445–449 (2018).
16. Neutzner, S., Srimath Kandada, A. R., Lanzani, G. & Petrozza, A. A dual-phase architecture for efficient amplified spontaneous emission in lead iodide perovskites. *J. Mater. Chem. C* **4,** 4630–4633 (2016).
17. Milot, R. L., Eperon, G. E., Snaith, H. J., Johnston, M. B. & Herz, L. M. Temperature-Dependent Charge-Carrier Dynamics in CH 3 NH 3 PbI 3 Perovskite Thin Films. *Adv. Funct. Mater.* **25,** 6218–6227 (2015).